Upstream ORFs control TNFR1 abundance and tissue tolerance to TNF

Authors: Biao Ma[1,2*], Wenxin Lyu[2], John Rizk[2], Xiaoyue Han[1], Majken Kjær[2], Vinnycius Pereira Almeida[1], Malin Jessen[2], Max Sauerland[2], Carol Sze Ki Leung[1,3], Benoit Van Den Eynde[1,4,5], Xin Lu[1], Mads Gyrd-Hansen[1,2*]

Affiliations:

[1]Ludwig Institute for Cancer Research, Nuffield Department of Medicine, University of Oxford; Oxford, UK

[2]LEO Foundation Skin Immunology Research Center, Department of Immunology and Microbiology, University of Copenhagen; Copenhagen, Denmark

[3]Centre for Immuno-Oncology, Nuffield Department of Medicine, University of Oxford; Oxford, UK

[4]Ludwig Institute for Cancer Research, de Duve Institute, UCLouvain; Brussels, Belgium

[5]WELBIO department, WEL Research Institute; Brussels, Belgium

*Corresponding author. Email: biao.ma@sund.ku.dk (B.M.); mgyrd@sund.ku.dk (M.G-H.)

Abstract: Tumor necrosis factor (TNF) orchestrates immune responses but can also drive inflammation-associated tissue damage. However, the mechanisms governing tissue tolerance to TNF remain poorly understood. Here, we reveal that TNF receptor 1 (TNFR1) abundance is regulated by two upstream open reading frames (uORFs) in the 5′ untranslated region of *TNFRSF1A* and demonstrate that this is a key determinant of TNF tolerance. uORF2 dominantly limits TNFR1 translation and its disruption increases TNFR1 levels, leading to excessive TNF-induced gene activation and cell death in cell culture, whereas uORF1 dynamically regulates TNFR1 levels in response to inflammatory and stress signals. In mice, uORF2 protects against TNF-driven systemic inflammatory response syndrome and liver pathology. Additionally, the translation of other immune receptor mRNAs, including *TLR4*, *IFNAR1*, and *IFNGR2,* is controlled by uORFs. Thus, regulation of TNFR1 levels and possibly of other immune receptors emerges as a mechanism safeguarding against excessive immune responses and tissue damage.

One-Sentence Summary:

Upstream open reading frames exert translational control of TNF Receptor 1, thereby limiting tissue responsiveness to TNF.

Keywords: TNFR1, uORFs, mRNA translation, inflammation, cell death

Main text:

INTRODUCTION

Inflammation is an essential host-protective mechanism against infection but can also cause severe acute and chronic pathology when dysregulated or excessively activated, as is the case in the systemic inflammatory response syndrome (SIRS) and sepsis where inflammation may lead to organ damage and lethality (*1*). Inflammation relies on immune receptors that in response to activation by their cognate ligands trigger intracellular signaling events that coordinate subsequent immune responses (*2, 3*). Tumor necrosis factor (TNF), a pleiotropic proinflammatory cytokine, signals through TNF receptor 1 (TNFR1) and 2 (TNFR2) to orchestrate inflammatory responses by activating receptor signaling pathways mediated by mitogen-activated protein kinase (MAPK) and nuclear factor kappa B (NF-κB). TNFR1 mediates most of the inflammatory effects of TNF (*4*) and can in some circumstances also trigger programmed cell death, which itself can promote inflammation through the release of inflammatory mediators (*5, 6*). Dysregulation of TNF-induced signaling in tissues contributes to chronic inflammatory and autoimmune diseases (*4, 7*), underscoring the importance of properly regulated tissue responses to TNF to ensure effective immune responses without excessive tissue damage (*8*).

TNFR1 signaling is regulated by several mechanisms to balance NF-κB-mediated gene activation and cell death (*7*). Upon TNF binding, TNFR1 assembles a membrane-bound signaling complex (complex I) wherein the ubiquitin ligases cellular inhibitor of apoptosis 1 (cIAP1) and 2 (cIAP2), and linear ubiquitin chain assembly complex (LUBAC) conjugate nondegradative ubiquitin chains on receptor-interacting serine/threonine-protein kinase 1 (RIPK1), TNFR1 and other receptor-associated components. This facilitates recruitment and activation of the kinases inhibitor of kappa-B kinase (IKK) and TGF-β-activating kinase 1 (TAK1) that activate MAPK and NF-κB signaling to induce gene activation and suppress cell death signaling (*6*). Ubiquitination and activation of kinases at the TNFR1 complex I engages checkpoints that prevent activation of RIPK1 and excessive formation of a cytosolic cell death-inducing complex (complex II) composed of RIPK1, Fas-associated death domain protein (FADD), and caspase-8 that can induce apoptosis, necroptosis, or pyroptosis depending on the context (*6*). Additionally, NF-κB target genes such as *TNFAIP3* and *NFKBIA* provide feedback inhibition to restrict TNFR1 signaling (*10-12*). Genetic mutations that affect the folding and shedding of TNFR1 indicate that dysregulation of TNFR1 itself can lead to TNF-mediated pathology, as observed in TNF receptor–associated periodic fever syndrome (TRAPS) and in mice with mutation of the cleavage site for disintegrin and metalloproteinase 17 (ADAM17) in TNFR1 (*13, 14*). The regulatory mechanisms that operate downstream of TNFR1 activation have been extensively studied, but much less is known about the cellular mechanisms that regulate the abundance of TNFR1 and how these affect inflammatory signaling.

Here, we uncover an evolutionarily conserved mechanism that limits TNFR1 abundance to restrain TNF-driven inflammation. Two upstream open reading frames (uORFs) in the *TNFRSF1A* 5′ untranslated region (5′ UTR) restrict TNFR1 translation and limit TNF-induced gene activation and cell death in cell culture and in vivo. We show that uORF-mediated control of TNFR1 is regulated by cytokines such as TNF and IL-1β, and by microenvironmental stressors. Finally, we identify a patient-linked SNP, rs115164694 (−96C>T) that creates a neo-uORF and reduces TNFR1 translation, and we provide evidence that translation of other immune receptors is restricted by uORFs. Our study uncovers a critical role for uORFs in maintaining immune homeostasis and suggests their contribution to inflammatory disease when dysregulated.

RESULTS

A conserved uORF in *TNFRSF1A* restricts translation of TNFR1

The 5′ UTR of mRNAs harbors functional elements that regulate the translation of the protein coding sequence (CDS) (*13*). Through sequence alignment of *TNFRSF1A* from multiple species we noticed an evolutionarily conserved region in the 5′ UTR near the start codon of the CDS (Fig 1A). The region harbors a 12-bp upstream open reading frame (uORF, referred to as uORF2 hereafter) starting at position −31 and terminating at position −20 relative to the CDS initiation site (Fig 1A). The human *TNFRSF1A* 5′ UTR additionally harbors a longer uORF (denoted uORF1) at positions −141 to −10, which overlaps with uORF2 but in a different reading frame (Fig 1A). To determine whether the uORFs in *TNFRSF1A* were recognized by ribosomes, we used GWIPS-viz (*15*) to analyze publicly available initiating ribosome profiling data from cell lines (*16-23*). This revealed that both uORF1 and uORF2 contain functional AUG start codons (Fig. 1B). To compare how each uORF regulates TNFR1 translation, we generated a GFP reporter in which the *TNFRSF1A* 5′ UTR was placed upstream of GFP and individually mutated the start codon of uORF1 and uORF2 (fig. S1A). Transient transfection of the constructs into HCT116 human colon cancer cells revealed that uORF2 plays a dominant role in restricting TNFR1 translation (as measured by GFP fluorescence), whereas mutation of uORF1 had only a modest effect (fig. S1B).

The impact of uORF2 on translation of the CDS was further validated by additional point mutations in its start codon (−31A>U, −30U>G, −29G>A), which showed that ablation of uORF2 enhanced GFP levels by four- to five-fold compared to the wildtype (WT) construct (Fig. 1C). Conversely, mutation of the stop codon (−20A>U), thereby creating a uORF2 that extends beyond the CDS in a different reading frame to GFP, strongly reduced the level of GFP (Fig. 1C). Altering the stop codon from UGA to UAA or UAG did not affect GFP levels (Fig 1C). Thus, the translation of the *TNFRSF1A* CDS is attenuated by uORF2, which may depend on ribosome reinitiation at the CDS start codon following translation of uORF2. The efficiency of ribosome reinitiation is inversely correlated with the length of uORFs (*24*). In line with this, GFP was not detected when the length of uORF2 was increased by fusing it with an RFP-coding sequence (fig. S1, C and D).

We next examined how uORF2 controls endogenous TNFR1 translation by generating two HCT116 clones with disrupted uORF2 start codons (fig. S1, E and F). Both mutants displayed increased total and surface TNFR1 protein compared with WT cells (Fig. 1, D and E), despite having lower *TNFRSF1A* mRNA levels (fig. S1G). One clone (Δu/Δu) carried a homozygous start-codon mutation, whereas the second clone (Δu/+G) was deleted for uORF2 on one allele and harbored a frameshift in the remaining uORF2 allele, extending the uORF into the CDS (fig. S1F). Consistent with impaired translation from this allele, TNFR1 levels in Δu/+G were intermediate between WT and Δu/Δu cells. To test whether elevated TNFR1 abundance was due to increased translation, we measured de novo protein synthesis using L-azidohomoalanine (L-AHA) labeling (fig. S1H). uORF2 mutation selectively enhanced TNFR1 synthesis without affecting global translation or synthesis of RelA or S6 (Fig. 1F), with Δu/Δu showing the strongest effect.

To assess this mechanism in vivo, we generated uORF2-mutated mice that harbor a 2-base pair deletion of the uORF2 start codon ($Tnfrsf1a^{\Delta uORF2/\Delta uORF2}$, for simplicity referred to as uORF2$^{-/-}$; Fig. 1G and fig. S1I). Whole-genome sequencing confirmed that no predicted off-target mutations were introduced (data file S1). Primary dermal fibroblasts (MDFs) from uORF2$^{-/-}$ mice showed markedly increased total and surface TNFR1 (Fig. 1, H and I) and enhanced de novo TNFR1 synthesis (Fig. 1J), while *Tnfrsf1a* mRNA levels were unchanged (fig. S1J). Thus, uORF2 limits the translation and abundance of TNFR1 in both human and mouse cells.

uORF2-regulated TNFR1 abundance is rate-limiting for TNF signaling outcomes

To investigate how uORF2-mediated regulation of TNFR1 abundance shapes cellular TNF responses, we initially examined TNFR1 complex I. TNFR1- and LUBAC activity-deficient (*TNFRSF1A*-KO and *RNF31*-KO) cells confirmed that TNF signals through TNFR1 and required LUBAC for Met1-Ub formation (Fig. 2A). uORF2-mutated HCT116 cells showed increased ubiquitinated TNFR1 and RIPK1, along with elevated Met1-linked ubiquitin (Met1-Ub) (Fig. 2A). Productive TNF signaling as determined by IL-8 production was accordingly enhanced in uORF2-mutated cells relative to WT cells (Fig. 2B and fig. S2A). In contrast to the enhanced TNF-induced IL-8 production in uORF2-mutated cells, IL-1β–induced IL-8 production was slightly reduced (fig. S2, B and C), indicating that the effect of the uORF2 mutation is specific to TNF.

Despite heightened NF-κB activation, which normally suppresses cell death (*25*), uORF2-mutated HCT116 cells were sensitized to TNF-induced cell death, displaying increased caspase-8 cleavage and caspase-3/7 activity (Fig. 2, C and D and fig. S2, D to F). Costimulation with TNF and interferon gamma (IFN-γ) further increased caspase activity and cell death in both WT and uORF2-mutated cells, a synergistic effect that was suppressed by the JAK1 inhibitor Ruxolitinib (Fig. 2C and fig. S2, D to F). Cell death induced by TNF plus IFN-γ was blocked by the pan-caspase inhibitor Z-VAD-FMK and the caspase-8 inhibitor Z-IETD-FMK (Fig. 2C and fig. S2E), showing that cells died by apoptosis. In accordance, the RIPK1-targeted necroptosis inhibitor Nec1s only modestly reduced cell death (Fig. 2C). TRAIL-induced cell death was comparable between uORF2-mutated and WT cells (fig. S2G), further confirming a TNF-specific phenotype.

Akin to uORF2-mutated cells, ectopic overexpression of TNFR1 sensitized to cell death by TNF and TNF plus IFN-γ (fig. S2, H and I). This suggests that elevated levels of TNFR1 increases both complex I and II formation, which may overload autophagy-mediated removal of active caspase-8 (*26*). Supporting this, the autophagy inhibitor bafilomycin A1 markedly enhanced the accumulation of cleaved caspase-8 p43/41 and p18 in uORF2-mutant cells compared to WT (Fig. 2D).

These findings were recapitulated in primary MDFs; uORF2$^{-/-}$ MDFs displayed elevated Met1-Ub, ubiquitinated TNFR1 and RIPK1 (Fig. 2E), enhanced phosphorylation of the NF-κB subunit RelA and NF-κB target gene induction (Fig. 2F and fig. S2J), and increased cell death (Fig. 2G) after TNF treatment relative to WT MDFs. Unlike HCT116 cells, MDFs can undergo necroptosis (*27, 28*). Mutation of uORF2 sensitized MDFs to necroptosis induced by TNF plus Z-VAD-FMK as determined by increased phosphorylation of RIPK1, RIPK3, and MLKL, and inhibition by Nec1s (Fig. 2, G and H). TNF alone induced weak RIPK1, RIPK3, and MLKL phosphorylation in uORF2$^{-/-}$ MDFs, but not in WT cells (Fig. 2H). Thus, uORF2-mediated limitation of TNFR1 abundance restricts TNF-induced gene induction and prevents cell death.

Increased level of TNFR1 caused immune dysregulation

We next examined the role of uORF2 in *Tnfrsf1a* in vivo. Disruption of uORF2 did not adversely affect embryonic development and neonatal viability since mice at weaning showed the expected mendelian ratios of genotypes (Fig. 3A and fig. S3A). uORF2$^{-/-}$ mice also gained weight at similar rates as their WT counterparts (Fig. 3B) and had normal blood parameters as determined by total white blood cells (WBCs), lymphocytes, red blood cells (RBCs), and hemoglobin (HGB) levels (fig. S3B). In line with cell culture data, uORF2$^{-/-}$ mice presented with increased levels of TNFR1 in multiple organs as compared with WT mice, particularly in the liver and intestine (Fig. 3C). uORF2 heterozygous mutant mice (uORF2$^{+/-}$) also showed increased TNFR1 levels (Fig 3C). uORF2$^{-/-}$ mice displayed increased spleen-to-body weight ratios as compared with WT littermates (Fig. 3D), and had increased numbers of splenic macrophages, monocytes, effector CD8 T cells, and central memory CD8 T cells. By contrast, splenic natural killer (NK) cell, NK1.1+ T cell, γδ T cell, and naïve CD4 T cell numbers were reduced relative to WT mice, whereas other immune cells detected were unaltered (Fig. 3E and fig. S3C). The liver-to-body weight ratio was also increased in uORF2$^{-/-}$ mice (Fig. 3F) and hematoxylin and eosin (H&E) staining indicated focal immune cell infiltrates in the livers (Fig. 3G). Staining for immune cell markers confirmed that these foci contained myeloid cells and lymphocytes (Fig. 3, G and H). Thus, although uORF2$^{-/-}$ mice do not display any overt pathology, the increased level of TNFR1 does result in immune dysregulation.

uORF2 limits TNFR1 levels in vivo to promote tolerance to TNF

We next challenged mice with TNF. WT C57BL/6 mice, which develop RIPK1-mediated lethal SIRS when administered TNF intravenously (*29*), were tolerant to intraperitoneal (i.p.) administration of TNF (Fig. 4, A and B) (*30, 31*). By contrast, uORF2$^{-/-}$ mice developed hypothermia within 2 to 4 hours of i.p. injection of TNF and became moribund, and uORF2$^{+/-}$ mice showed an intermediate response (Fig. 4, A and B). uORF2$^{-/-}$ mice concomitantly developed severe hypoglycemia with life-threateningly low blood glucose levels (*32*) (Fig. 4C). TNF also caused a transient reduction in blood glucose levels in WT mice, but this stabilized and was restored to almost baseline levels after 24 hours (Fig. 4C).

To elucidate how TNF causes pathology in uORF2$^{-/-}$ mice, we examined mice 2 hours after TNF administration, at which point the mice still had near-normal glycemic levels and body temperature (Fig. 4, A to C). Blood analyses showed normal WBC and lymphocyte counts, and a 1.2-fold increase in RBC counts and HGB levels after TNF, with no significant differences between WT and uORF2$^{-/-}$ mice (fig. S4, A to D). By contrast, uORF2$^{-/-}$ mice, but not WT mice, displayed increased plasma levels of alanine transaminase (ALT) and aspartate transaminase (AST) and had darkened livers in response to TNF, indicative of hepatic damage and hepatic congestion (Fig. 4, D to F, and fig. S4E). Livers from uORF2$^{-/-}$ mice showed vascular congestion, increased numbers of apoptotic hepatocytes, and areas positive for cleaved caspase-3 (Fig. 4G). Periodic acid–Schiff (PAS) staining indicated decreased glycogen levels in both WT and uORF2-mutant livers, consistent with the observed hypoglycemia (fig. S4F). In addition to liver damage, TNF caused extensive epithelial apoptosis in the intestines and moderate apoptosis in the kidney cortex of uORF2-mutant mice as determined by cleaved caspase-3 staining (fig. S5). The skin and spleen showed slightly increased cleaved caspase-3 positivity, whereas the heart and lungs were negative (fig. S5). Surfactant protein D (SP-D) levels in the plasma, an indicator of lung damage, did not change after TNF challenge (fig. S6A). The tissues of WT mice showed little to no cleaved caspase-3 staining in response to TNF (Fig. 4G and fig. S5).

uORF2$^{-/-}$ mice also exhibited enhanced immune signaling responses to TNF in comparison with WT mice as evidenced by elevated expression of NF-κB target genes *Tnf*, *Il1b*, and *Ccl2* in the liver (Fig. 4H) and increased plasma concentration of the inflammatory markers IL-6 and CXCL-1 (Fig. 4, I and J). Plasma TNF levels were comparable between genotypes, confirming that mice were exposed to similar doses of TNF (fig. S6B).

To determine the relative contributions of hematopoietic versus nonhematopoietic cells to TNF-induced SIRS and lethality of uORF2$^{-/-}$ mice, we performed bone marrow chimera experiments (fig. S7, A to C). Following TNF administration, uORF2$^{-/-}$ CD45.2 hosts reconstituted with WT CD45.1 hematopoietic cells recapitulated the TNF-sensitive phenotype of uORF2$^{-/-}$ mice (Fig. 4, A to C, and fig. S7, D to F). By contrast, WT CD45.1 hosts reconstituted with uORF2$^{-/-}$ hematopoietic cells remained tolerant to TNF (fig. S7, G to I). Thus, uORF2-mediated regulation of TNFR1 in nonhematopoietic cells is critical for tissue tolerance to TNF.

TNFR1 contributes to the acute pathology and hypothermia in murine models of lippopolysaccharide (LPS)–induced sepsis (*33*). To assess the impact of the increased levels of TNFR1 in uORF2$^{-/-}$ mice on the acute innate immune response to bacterial infection, we administered the peptidoglycan constituent muramyl dipeptide (MDP) i.p. to mice in order stimulate NOD2 (nucleotide-binding oligomerization domain–containing protein 2) signaling followed by LPS administration i.p. (*34*). uORF2$^{-/-}$ mice exhibited increased susceptibility to LPS-induced hypothermia and lethality (Fig. 4, K and L). Administration of a neutralizing anti-TNF antibody delayed LPS-induced hypothermia and prevented the acute lethality (Fig. 4, K and L). Thus, uORF2-mediated translational control of TNFR1 promotes tolerance to TNF during an acute immune response and thereby supports host fitness (fig. S8).

Translation of uORF2 facilitates leaky scanning, reducing initiation at the *TNFRSF1A* start codon

To dissect how uORF2 restricts TNFR1 translation, we used GFP reporters designed to monitor either uORF2 initiation or ribosomal leaky scanning to the CDS (Fig. 5, A and B). This revealed strong uORF2 translation but only minimal scanning past its start codon toward the CDS (Fig. 4C). Translation from the downstream ORF start codon at +209 was significantly higher than from the CDS. However, ablation of uORF2 increased translation of the CDS and reduced translation of the +209 ORF (Fig. 4C), suggesting that uORF2 promotes ribosome scanning past the CDS start codon. Enhancing start codon recognition by introducing an optimal Kozak sequence reduced leaky scanning and nearly abolished downstream translation, supporting mutually exclusive recognition of the +1 and +209 start codons by individual ribosomes. Kozak optimization decreased leaky scanning (2.2-fold) more than it increased main CDS translation (1.37-fold), indicating that initiation at +209 was more efficient than at +1.

Given the evolutionary conservation of uORF2 (Fig. 1A), we hypothesized that its sequence features contribute to reinitiation efficiency. To test this, we generated a series of uORF2 mutants (fig. S9A). Mutating the stop codon context (GGG>AAA) had no effect but a minimal uORF2 (MG) substantially impaired reinitiation at both +1 and +209, likely due to ribosome disassembly (fig. S9B). Substitution of uORF2 amino acids showed sequence-specific effects on translation of the CDS: MEE enhanced leaky scanning of the CDS start codon whereas MRR and MPE suppressed it and increased CDS translation. MPP had no effect on reinitiation at +1 but reduced reinitiation at +209 (fig. S9, A and B), suggesting that the uORF2 peptide sequence influences downstream reinitiation efficiency.

Although uORF2 plays a dominant role in restricting TNFR1 translation (fig. S1B), this does not exclude that uORF1 is recognized and translated by scanning ribosomes, which would affect utilization of uORF2 since translation of the two uORFs is mutually exclusive. Indeed, mutation of the uORF1 stop codon alone, or together with +1 start codon so GFP was exclusively translated from uORF1, increased GFP levels relative to the WT (+1) reporter, indicating that uORF1 is translated (Fig. 5, D and E). By comparison, translation of GFP from the uORF2 start codon (in the presence of the uORF1 start codon) was almost twice as efficient, indicating substantial leaky scanning of uORF1 (Fig. 5, D and E). In line with this, mutation of the +1 start codon in the uORF1 stop codon mutant reporter led to a decrease in GFP signal (uORF1 initiation versus uORF1 stop mut) that equated the GFP signal generated from the uORF2 reinitiation reporter (uORF2 REI) (Fig. 5, D and E).

To address why uORF1 is translated but has a weaker impact than uORF2 on translation of the CDS, we assessed the reinitiation efficiency following translation of uORF1 versus uORF2. This showed that uORF2 facilitated higher reinitiation efficiency than uORF1, consistent with the dominant role of uORF2 in regulating translation of the TNFR1 CDS (Fig. 5F). Because initiation at uORF1 and uORF2 are mutually exclusive, mutating the uORF1 start codon led to increased uORF2 translation and modestly enhanced reinitiation at both +1 and +209 sites (Fig. 5G). Initiation from non-AUG start codons contributed minimally to GFP translation when all AUG start codons were mutated (Fig. 5, D and E). Thus, uORF2 restricts the translation of the TNFR1 CDS by promoting leaky scanning at the CDS start codon. Furthermore, uORF2 utilization may be regulated by uORF1, which only poorly supports translation of the CDS.

A disease-associated SNP disrupts *TNFRSF1A* uORF regulation and reduces TNFR1 level

Searching the ClinVar database (*35*) for genetic variants in the 5′ UTR of *TNFRSF1A* that potentially would perturb uORF function led us to identify a SNP (rs115164694) reported in patients with TRAPS and other autoinflammatory syndromes. Although currently classified as of uncertain significance or likely benign (fig. S9C), this variant causes a −96C>U substitution in the 5′ UTR of *TNFRSF1A*, which creates a novel AUG start codon upstream of uORF2 and generates a neo-uORF within the uORF1 region (Fig. 5H and fig. S9D). This SNP has a global allele frequency of 0.068%, with higher prevalence in individuals of African descent (1.092%) (fig. S9E). Reporter assays showed that the neo-uORF is translated, enhancing uORF1 initiation but suppressing initiation at uORF2 and translation from the +1 and +209 start sites (Fig. 5, H and I). Given that uORF1 and uORF2 are mutually exclusive and that uORF1 has lower reinitiation efficiency, these changes likely account for the overall reduction in translation of the CDS. In accordance, stable expression of *TNFRSF1A* harboring either the WT or −96C>U 5′ UTR in *TNFRSF1A*-knockout (KO) HCT116 cells showed that the −96C>U variant led to lower TNFR1 protein levels despite comparable mRNA abundance (Fig. 5, J and K). This SNP may serve as a genetic determinant of TNFR1 levels in certain populations, potentially contributing to individual differences in TNF responsiveness. It also shares mechanistic similarities with known TRAPS-associated variants such as C43S in *TNFRSF1A*, which reduces total and surface TNFR1 levels (*36, 37*).

Stress induced selective translation of uORF1 inhibits uORF2-mediated TNFR1 translation reinitiation

Because uORF activity often correlates with the translational efficiency of the downstream CDS (*38*), we examined how global translational stress affects TNFR1 expression and signaling. Multiple stresses known to suppress protein synthesis, namely hypoxia, dimethyloxalylglycine (DMOG), carbonyl cyanide m-chlorophenyl hydrazone (CCCP), and UVB exposure each caused near-complete depletion of TNFR1 within 24 hours (*39-42*) (fig. S10, A to C), indicating that TNFR1 abundance is highly sensitive to reduced translation. Consistently, cycloheximide chase experiments showed that TNFR1 has a short half-life of ~2 hours (fig. S10, D and E). Hypoxia, a physiologically relevant stress (*43*), markedly reduced TNFR1 levels in diverse human cell lines and primary MDFs without proportional loss of *TNFRSF1A* mRNA (Fig. 6, A and B, and fig. S10, F to L), leading to blunted TNF signaling across multiple readouts (Fig. 6, A to D, and fig. S11, A to C). Other core components of the TNFR1 signaling complex remained stable during 24 hours of hypoxia, highlighting a selective sensitivity of TNFR1 to translational stress (fig. S10B). Hypoxia also attenuated TNF-induced gene activation in human organoids and protected HT29 cells from TNF-induced necroptosis (fig. S11, D and E). These effects were not explained by enhanced TNFR1 turnover, as blocking proteasomal, lysosomal, TNFR1 internalization or metalloprotease-mediated turnover failed to restore TNFR1 levels (fig. S11F). Importantly, returning cells to normoxia rapidly restored TNFR1 abundance and TNF responsiveness (fig. S11G), indicating that hypoxia suppresses TNFR1 primarily through reduced translation rather than altered protein stability. In line with the dominant role of uORF2 in restricting TNFR1 levels, uORF2-mutated HCT116 cells and primary MDFs retained TNFR1 levels under hypoxic conditions that were comparable to or higher than those of WT cells under normoxia (Fig. 6, A and B). Consequently, hypoxia attenuated TNF signaling responses in uORF2-mutated cells to a lesser degree than in WT cells (Fig. 6, A, C, and D, and fig. S11H). Thus, uORF2 links environmental stress to reduced TNFR1 translation and attenuated TNF responsiveness.

To dissect how uORFs regulate TNFR1 translation during hypoxia, we quantified initiation at uORF1 and uORF2, reinitiation at the CDS (+1 start codon), and leaky scanning in reporter assays. Hypoxia suppressed global translation and reduced GFP levels across constructs (Fig. 6E and fig. S12A). However, uORF1 initiation and +1 CDS translation in uORF2-mutant reporters were less affected (Fig. 6E), and the +1 CDS/+209 ORF ratio remained unchanged (fig. S12B). Hypoxia increased the uORF1/uORF2 initiation ratio (Fig. 6F), aligning with reduced reinitiation at the +1 start codon after translation of uORF1 relative to uORF2 (Fig. 5F). DMOG produced similar responses (fig. S12, C to E).

To evaluate if *Tnfrsf1a* uORF usage would be regulated by immunological cues we tested a panel of receptor ligands. This revealed that the proinflammatory cytokines TNF and IL-1β markedly reduced GFP levels from the +1 start codon in the WT 5′ UTR reporter (Fig. 6G), whereas IFNs, IL-6/sIL-6R, TGF-β, or L18-MDP had little effect. Combining TNF plus IFNs treatment counteracted the repression by TNF alone, implying signaling crosstalk between these pathways (Fig. 6G). Phosphorylation of eukaryotic initiation factor 2 (p-eIF2) suppresses translation in response to cellular stress by inhibiting eIF2B (*44*). However, the eIF2B activator 2BAct (*45*) did not rescue TNF-mediated translational repression , indicating that p-eIF2 is not involved (Fig. 6G).

TNF and IL-1β, alone or in combination, increased uORF1 initiation and reduced uORF2 initiation (Fig. 6, H and I), elevating the uORF1/uORF2 ratio (Fig. 6J), and decreased endogenous TNFR1 protein without altering mRNA levels (Fig. 6K and fig. S12F). IL-1β pretreatment lowered TNF-induced IL-8 production in both WT and uORF2-mutant cells, albeit uORF2-mutant cells remained more responsive (Fig. 6L and fig. S12, G and H). uORF1 start-codon mutation modestly increased basal +1 translation but did not fully prevent TNF-mediated repression (fig. S12I), suggesting that additional mechanisms influenced this. Indeed, we noted a modest reduction in the +1/+209 translation ratio (fig. S12J), suggesting increased leaky scanning at the +1 start codon in response to TNF and/or IL-1β. Also, TNF and/or IL-1β mildly increased non-AUG initiation (fig. S12K).

In line with our data, published ribosome-profiling data from HCMV-infected human fibroblasts (*46*) and LPS-stimulated mouse dendritic cells (*47*) revealed decreased ribosome occupancy at uORF2 and increased occupancy at the 5′ end of uORF1 (Fig. 6M). Thus, the translational efficiency of uORF1 is influenced by cellular stress and certain cytokines, which consequently reduces uORF2 utilization and reinitiation at the main CDS of *TNFRSF1A* (Fig. 6N).

uORFs negatively regulate the translation of several immune receptors

In addition to *TNFRSF1A*, several other immune receptor genes harbor one or more uORFs, particularly those encoding pattern recognition receptors (PRRs) and cytokine receptors, whereas genes encoding chemokine and complement receptors contain fewer uORFs (Fig. 7A and data file S2). Most uORFs identified in these genes are fully located within the 5′ UTR, whereas the remainder overlap the CDS or contain mixed uORF types (Fig. 7B and data file S2), suggesting that differential uORF recognition may broadly influence the translation of immune receptors. Analysis of initiating ribosome profiling data for the single-uORF-containing genes *TLR4*, *IFNAR1*, and *IFNGR2* suggested that the AUG codons of these uORFs are recognized as translation initiation sites and thus may limit translation of their respective CDS (Fig. 7, C to E). Indeed, 5′ UTR-GFP reporter assays demonstrated that WT constructs containing these uORFs yielded 80 to 85% lower GFP levels than their respective uORF-mutant constructs (Fig. 7, F to H). Thus, uORF-mediated translational control may be a broader regulatory strategy for modulating immune receptor levels and immune activation.

DISCUSSION

TNF is critical for the host defense to infections but also drives immune-mediated inflammatory pathology (*7*). The pathophysiology of TNF signaling is extensively studied in relation to the immune cell types producing TNF and to the signaling mechanisms activated by TNFR1 in responding cells and tissues (*6, 48*). Our study now adds TNFR1 abundance, controlled by uORFs, as a critical determinant of the cellular and tissue-wide sensitivity to TNF.

In addition to activation of genes encoding pro-inflammatory mediators, TNF-induced cell death has emerged as a driver of pathological inflammation (*5, 6*). Normally, the cell death pathway downstream of TNFR1 is only activated when check points are disabled through genetic-, pharmacological-, or pathogen-mediated manipulation. Our data show that increased abundance of TNFR1 without perturbation of the intracellular signaling pathway is sufficient to induce cell death, particularly when cells are sensitized by co-stimulation with IFNγ. Mechanistically, the increased accumulation of processed caspase-8 in uORF2-mutated cells when autophagy was inhibited, implies that the capacity of the autophagy-mediated cell death check point (*26*) is limiting for the removal of active caspase-8 from the cytosol. Investigations of how the capacity of this checkpoint is regulated may uncover molecular mechanisms that can modulate TNF cytotoxicity in tissues with high TNFR1 levels.

The lack of overt immune pathology of uORF2$^{-/-}$ mice contrasts the autoimmune-like disease in mice with constitutively elevated TNF levels due to deletion of the AU-rich elements in the 3′ UTR of the *Tnf* mRNA (*49, 50*). This likely reflects that under unchallenged conditions, the TNF levels are limiting relative to the signaling capacity of TNFR1, at least under specific pathogen-free (SPF) animal housing conditions. Conversely, the acute pathology of uORF2$^{-/-}$ mice in response to TNF or LPS plus MDP challenge indicates that TNFR1 abundance becomes limiting for TNF responses during acute immune stimulation. This highlights non-redundant layers of ligand- and receptor-level control that collectively modulate TNF-mediated inflammatory thresholds.

uORFs serve a regulatory role as is described for translation of the stress-induced transcription factor ATF4. Although the uORF2-mediated translational regulation of TNFR1 by promoting leaky scanning of the CDS start codon differs from the uORF-mediated control of ATF4 translation (*51*), both cases highlight how uORFs can modulate start codon recognition and thereby regulate protein synthesis. Hypoxia or cytokine treatment did not affect leaky scanning of the TNFR1 CDS start codon, but we speculate that other microenvironmental cues may regulate leaky scanning to modulate the translation of TNFR1.

Our finding that the patient-linked SNP (rs115164694, −96C>T) generates a neo-uORF that reduced TNFR1 translation by disrupting normal uORF1/2 utilization, adds supports for the central role of uORFs in regulating TNFR1 abundance and autoinflammatory risk. Although the clinical significance of this variant remains unresolved, our findings suggest that 5′ UTR variants should be considered alongside known *TNFRSF1A* coding mutations in TRAPS (*14*). Larger genetic and population-based studies will be required to determine whether this SNP constitutes a disease-risk allele and a clinical biomarker.

A limitation of our study is that whilst ablation of uORF2 in *Tnfrsf1a* increased TNFR1 levels in multiple tissues, it remains to be determined if this applies to all cells uniformly within the tissue. Our study also does not address if the reduction in TNFR1 levels in cultured cells after exposure to microenvironmental cues such as hypoxia and cytokines, also applies to tissues in vivo. It is tempting to speculate that TNFR1 abundance in tissues may be fine-tuned by the variable local oxygen tension and during tissue inflammation. Our data defines the mechanistic framework of uORF-function in *Tnfrsf1a* and other uORF-containing immune receptor genes using reporter systems, but a deeper molecular understanding will require elucidating how ribosomes are recruited and regulated at these uORFs. We also cannot exclude potential roles for RNA modifications or additional translation factors in shaping uORF selection (*52, 53*).

In summary, our study shows that uORFs act as a tunable translational checkpoint that restricts TNFR1 production to prevent TNF toxicity, and points to uORFs as a broader principle for limiting immune receptor abundance and preserving immune homeostasis.

MATERIALS AND METHODS

Mice

TNFRSF1A uORF2-mutant mice were generated by the Transgenic Core Facility at the University of Copenhagen. Briefly, sgRNAs targeting TGGCCTCTCACTCCCCCATT were coinjected with Cas9 protein into zygotes from C57BL/6NRj mice. Genotyping was performed by PCR amplification followed by confirmation using Sanger sequencing with the following primers: Forward: GCTCATGATCGGGCCTACTG; Reverse: CCCTCCAGTCTCCCATCTCA. Mice used in experiments were 7 to 12 weeks of age. They were maintained in a specific pathogen–free facility. ARRIVE guidelines were followed and all animal experiments were performed in accordance with protocols approved by the Institutional Animal Care and Use Committee of the University of Copenhagen (2021-15-0201-00919).

Injections, monitoring, and sampling

In the TNF-induced SIRS model, mice received i.p. injection of 250 µg per kilogram of body weight of carrier-free recombinant mouse TNF (BioLegend, 575208) diluted in PBS to a volume of 0.1 ml. Within each genotype, mice were randomized to receive TNF or placebo injections. In the LPS-induced sepsis model, uORF2-mutant mice were randomized and 200 µg of neutralizing anti-TNF antibody (BP0058, Bio X Cell, Clone XT3.11) or isotype control antibody (BP0088, Bio X Cell, Clone HRPN), diluted in PBS to a volume of 0.2 ml, was administered i.p. After 24 hours, 5 mg per kilogram of body weight of MDP (MCE, HY-127090) in PBS was injected i.p. in a volume of 0.1 ml. Four hours after MDP administration, 10 mg per kilogram of body weight of LPS from *Escherichia coli* O111 (Merck, L2630) diluted in PBS was administered i.p. Rectal body temperature was measured using a rodent thermometer (BIOSEB, BIO-TK8851). A final body temperature below 27 °C was considered to meet the humane endpoint, at which point mice were euthanized and recorded as deceased. Glucose levels were assessed with a glucose meter (Accu-Chek Guide Me, Roche) by collecting blood directly onto a glucose test strip. Plasma and tissue samples were collected at specified time points after treatment.

Hematological analysis and plasma protein measurements

Numbers of white blood cells, lymphocytes, red blood cells, and hemoglobin levels were analyzed by an automated hematology analyzer (Sysmex). Quantification of cytokines, chemokines, ALT, AST, and SP-D was performed using ELISA, according to the manufacturers' instructions. The following ELISA kits were used: Mouse SP-D ELISA Kit (ab240683, Abcam), Mouse AST ELISA Kit (ab263882, Abcam), Mouse ALT ELISA Kit (ab282882, Abcam), Mouse CXCL1/KC DuoSet ELISA (DY453-05, Novus Biologicals), Mouse IL-6 DuoSet ELISA (DY406, Novus Biologicals), and Mouse TNF-alpha DuoSet ELISA (DY410, Novus Biologicals).

Bone marrow transplantation

Recipient mice received total body irradiation at the dose of 9 Gy, delivered in two fractions of 4.5 Gy each, one in the morning and one in the evening. On the following day, mice were reconstituted via tail vein injection with 1×10^7 autologous bone marrow cells isolated from either WT or genetically modified donor mice. Recipient mice were maintained for at least 8 weeks post-transplantation to allow full hematopoietic reconstitution. Reconstitution efficiency was assessed by flow cytometric analysis of peripheral blood, using CD45.1 and CD45.2 staining to distinguish donor- and host-derived cells.

Generation of primary mouse dermal fibroblasts (MDFs)

Mice aged 8 weeks were euthanized, and the entire tail was dissected and sequentially rinsed with iodophor, 70% ethanol, and PBS. The skin was dissected and incubated in digestion buffer overnight (12 to 18 hours) at 4°C. Following incubation, the skin was washed with PBS containing penicillin, streptomycin, and amphotericin B to remove residual dispase II. The dermis was then separated, cut into 0.5 to 1 mm pieces, and plated onto a 10-cm dish with the fat followed by incubation at 37°C with 5% CO_2 for 4 hours. After incubation, 8 ml of culture media heated to 37°C was added to the dish, and culturing continued for 7 to 10 days until fibroblast cells migrated from the tissue. The culture media was replaced every 3 days. MDFs were maintained in culture media containing DMEM/F12 (Fisher Scientific, 11504436), 15% FBS, 100 U/ml of penicillin–streptomycin, 250 ng/ml of amphotericin B, 50 μM β-mercaptoethanol, and 1 mM sodium pyruvate. The digestion buffer comprised 4 mg/ml of dispase II (Merck, D4693) dissolved in culture media.

Generation of human duodenal organoids

Duodenal biopsies were obtained from outpatients during endoscopy at the John Radcliffe Hospital, Oxford, with informed consent (approved by the Yorkshire & The Humber – Sheffield Research Ethics Committee: 16/YH/0247 and the South Central - Oxford C Research Ethics Committee: 09/H0606/78). Duodenal tissues were cut into 2- to 5-mm² fragments, washed with PBS, and incubated in 5 mM EDTA-PBS at 4°C for 15 min, followed by TrypLE digestion at 37°C for 30 min. The tissue fragments were then triturated to release cells, filtered through a 70-μm strainer, and centrifuged. The cell pellet was suspended in GFR basement membrane matrix (Corning, 354230), seeded in 24-well plates, and incubated at 37°C with organoid media containing 10 μM Y-27632 (StemCell Technologies, 72308) and 3 μM CHIR99021 (StemCell Technologies, 72054). Organoids were passaged weekly at a 1:4 ratio, with the media refreshed every other day. HEK293T Rspo1-Fc, HEK293T Nog-Fc, and L- Wnt3A cells were used to generate R-Spondin, Noggin and Wnt3A conditioned media, respectively. The culture medium for human duodenum organoids consisted of 50% Wnt3A, 30% R-Spondin and 20% Noggin conditioned media, with 10 mM HEPES buffer (pH 7.0). Additional supplements included 1X B-27 (Thermo Fisher Scientific, 17504001), 1X N-2 (Thermo Fisher Scientific, 17502001), 1 mM N-acetyl-L-cysteine (Merck, A9165), 10 nM gastrin (Merck, G9145), 500 nM A83-01 (StemCell Technologies, 72024), 10 µM SB202190 (StemCell Technologies, 72632), 10 mM nicotinamide (Merck, N3376), 100 ng/ml FGF10 (PeproTech, 100-26-25), and 50 ng/ml EGF (Thermo Fisher Scientific, PHG0311).

Cell culture, plasmids, and transfection

HCT116, Caco-2, SW48, LS-174T, HEK293T, and HT29 cell lines were obtained from the American Type Culture Collection (ATCC), and the GP2d cell line was from the European Collection of Authenticated Cell Cultures (ECACC). All cell lines were cultured under conditions specified by the supplier and were regularly tested as free from mycoplasma contamination using the MycoAlert Mycoplasma Detection kit (Lonza). A hypoxic condition was achieved by using a hypoxia workstation that maintained the culture conditions at 1% O_2, 5% CO_2, and 94% N_2. Mutations were introduced by site-directed mutagenesis using the QuikChange Lightning Kit (Agilent Technologies). The constructs and mutagenesis were confirmed via Sanger Sequencing. Plasmids were transfected into cells using FuGENE 6 transfection reagent (Promega, E2692) according to the manufacturer's protocols.

Generation of cell lines

To generate uORF mutant cells, oligonucleotides were cloned into lentiCRISPR v2 between the BsmBI sites. Lentiviral packaging plasmids, psPAX2 and pMD2.G, were cotransfected with the backbone plasmid into HEK293T cells for 48 hours to produce lentivirus. Target cells were infected with the virus in the presence of 8 µg/ml of polybrene for 24 hours, followed by selection with 1 µg/ml of puromycin in the culture media. For gene knockout, sgRNA against *TNFRSF1A* (Forward: CACCGAGAGGTGCACGGTCCCATTG; Reverse: AAACCAATGGGACCGTGCACCTCTC) was cloned into pSpCas9(BB)-2A-GFP (PX458). HCT116 cells were transiently transfected with the plasmids, and GFP^+ cells were subjected to single-cell sorting. TNFR1 knockout was confirmed by immunoblotting, functional assays, and sequencing. HOIP KO HCT116 cells are previously described (*54*). For uORF editing, sgRNAs targeting GFP (Forward: CACCGGAAGTTCGAGGGCGACACCC; Reverse: AAACGGGTGTCGCCCTCGAACTTCC) and uORF2 of *TNFRSF1A* (Forward: CACCGTGGCCTCTCACTCCCCCATT; Reverse: AAACAATGGGGGAGTGAGAGGCCAC) were cloned into lentiCRISPR v2 accordingly. The reconstructed lentiCRISPR v2 plasmids were used to produce lentivirus to generate cells expressing Cas9 with a puromycin resistance gene, which were selected by 1 µg/ml of puromycin for 1 week and then subjected to single-cell sorting. Gene editing was confirmed by immunoblotting, functional assays, and sequencing.

Reagents

Recombinant human TNF (PeproTech, 300-01A), biotinylated human TNF (Fisher Scientific, 15877837), recombinant murine TNF (PeproTech, 315-01A), biotinylated murine TNF (Fisher Scientific, 15807847), recombinant human IFN-β (PeproTech, 300-02BC), recombinant human IFN-γ (PeproTech, 300-02), recombinant human IL-1β (Fisher Scientific, 17810723), recombinant soluble human IL-6R (Fisher Scientific, 17801073), recombinant human IL-6 (Fisher Scientific, PHC0065), recombinant human TGF- β1 (R&D systems, 240-B-002/CF), recombinant human soluble TRAIL (PeproTech, 310-04), L18-MDP (Invivogen, tlrl-lmdp), Ruxolitinib (Cayman chemical, 11609), Z-IETD-FMK (Invivogen, inh-ietd), Z-VAD-FMK (MCE, HY-16658B), Nec-1s (Fisher Scientific, 17215270), 2BAct (MCE, HY-125021), DMOG (MCE, HY-15893), CCCP (MCE, HY-100941), MG132 (Selleck chem, S2619), Bafilomycin A1 (Merck, B1793), Cycloheximide (Merck, C4859), Chloroquine phosphate (Merck, PHR1258), Compound A (a kind gift from Tetralogic Therapeutics), GI254023X (Merck, SML0789), and TAPI-2 (Merck, SML0420).

Flow cytometry analysis

To analyze surface TNFR1 expression, cells were trypsinized, washed with PBS, and surface-stained with the designated TNFR1 antibodies in FACS buffer (PBS containing 2% FBS) on ice for 30 min. To analyze intracellular IL-8 production, cells were treated with monensin (1:1000, BD, 554724) for 1 hour, followed by the respective stimulation for an additional 3 hours. The cells were then harvested by trypsinization, washed with PBS, and fixed with 4% fixation buffer (BioLegend, 420801) at room temperature for 15 min. Cells were permeabilized and stained with an anti-IL8 antibody in permeabilization wash buffer (BioLegend, 421002) at room temperature for 30 min. To analyze the immune landscape of mouse spleens, extracted spleens were minced and digested with 500 µg/ml of collagenase IV and 20 µg/ml of DNase I on a magnetic stirrer at 37°C for 30 min. Cells were filtered using a 70-µm strainer and were lysed in RBC lysis buffer (BioLegend, 420301) on ice for 5 min. Cells were then filtered a second time using a 40-µm strainer, and cell numbers were counted. A total of 2.5×10^6 cells per sample were first blocked with anti-mouse CD16/CD32 antibody (1:100, BD, 553142, clone 2.4G2) on ice for 30 min before staining. The cells were then washed with FACS buffer, stained with designated antibodies on ice for 30 min, filtered using a 40 µm strainer, and resuspended in 200 µl FACS buffer. DAPI (1 µg/ml) (Merck, MBD0015) was added shortly before the samples were analyzed by a BD LSRFortessa™ Cell Analyzer or LSRFortessa™ X-20 Cell Analyzer. Repeated experiments were performed on the same flow cytometer with the same settings. Data processing was performed using FlowJo v10 software (FlowJo, LLC). More detailed information on the antibodies used is available in table S1.

Histology and immunohistochemistry

Tissues were fixed with 10% formalin, embedded in paraffin, sectioned at 4 µm, and stained with hematoxylin and eosin. For immunohistochemistry, slides were rehydrated and then treated with sodium citrate buffer (pH 6.0) (Akoya, AR6001KT) heated for 10 min at 95°C. The samples were treated with 0.3% H_2O_2 for 15 min to block endogenous peroxidase activity and then blocked with blocking reagent (Blocking One Histo, 06349-64) for 10 min at room temperature. The tissues were incubated with the indicated antibodies at 4°C overnight, followed by incubation with corresponding HRP-conjugated secondary antibody for 30 min at room temperature. The immunoreactive signal was visualized with a Metal Enhanced DAB Substrate Kit (Thermo Fisher Scientific, 34065). More detailed information on the antibodies used is available in table S2.

Cell viability assay and evaluation of cell death

Cells were cultured in 96-well plates to approximately 80% confluency. Cell viability was assessed using the CellTiter-Glo® 2.0 Cell Viability Assay (Promega, G9242) according to the manufacturer's instructions. For cell death assays, cells were seeded in 48-well plates in 350 µl of culture media supplemented with either 100 nM Sytox Green or 250 nM YOYO-3. The following day, cells were pre-treated with the indicated drugs in 50 µl of culture media for 1 hour, followed by stimulation with the indicated cytokines delivered in 1 µl of PBS. Real-time cell death was quantified based on Sytox Green–positive cell numbers, normalized to cell confluency. End-point cell death measurements were based on YOYO-3 positivity, normalized to Syto 21 positivity, which was added to the culture media 1 hour prior to analysis. For detection of activated caspase-3/7 together with cell death, the CellEvent™ caspase-3/7 detection reagent (red fluorescence; Thermo Fisher Scientific, C10430) was multiplexed with 100 nM Sytox Green in accordance with the manufacturer's instructions. Fluorescence signals were acquired using the IncuCyte S3 Live-Cell Analysis System (Sartorius).

Reporter assay based on fluorescence and luminescence

Reporter plasmids containing either the WT or mutant 5′ UTR of immune receptor genes, positioned upstream of an *EGFP* coding sequence, were transfected into cells under the control of a CMV promoter. For internal normalization, either an IRES-driven mCherry was included on the same plasmid or a CMV-driven DsRed or Renilla luciferase plasmid was cotransfected. Treatments were applied one-hour post-transfection. For constructs carrying both EGFP and mCherry, or involving cotransfected internal controls (DsRed), fluorescence intensities were quantified 24 hours post-transfection using the IncuCyte S3 Live-Cell Analysis System (Sartorius). For assays involving cotransfected internal controls (Renilla), GFP fluorescence and Renilla luminescence signals were measured using a CLARIOstar Plus plate reader (BMG Labtech) at the same time point.

Immunoblotting

The same numbers of cells were lysed in lysis buffer (1X loading buffer diluted with 1% SDS) and immediately heated at 100°C for 15 min. Equivalent volumes were subjected to SDS-PAGE and transferred to nitrocellulose membranes and then blocked with 5% nonfat milk or 1% BSA for 1 hour at room temperature. Membranes were then incubated with the indicated primary antibodies overnight at 4°C, followed by the appropriate HRP-conjugated or fluorescent dye–conjugated secondary antibodies. Immunoreactive bands were visualized with chemiluminescence kits or fluorescence using a ChemiDoc Imaging System. For quantification of GFP and RFP expressions related to hypoxic conditions, fluorescence-based immunoblotting was used, as the maturation of the respective chromophores requires oxygen (*55*). More detailed information on the antibodies used is available in table S3.

Immunofluorescence

Cells were fixed in 4% paraformaldehyde diluted in PBS for 15 min at room temperature, and then permeabilized with 0.1% Triton X-100 along with DAPI at 4°C. After blocking with goat serum for 30 min, cells were incubated with anti-RelA (1:400, 0.52 μg/ml) (Cell Signaling Technology, 8242, clone D14E12) for 1 hour at room temperature, washed three times with PBS, and incubated with FITC-conjugated secondary antibodies (1:1000) (Thermo Fisher Scientific, 31584) for 1 hour at room temperature. Slides were then washed three times with PBS and mounted using ProLong™ glass antifade mountant (Thermo Fisher Scientific, P36980). Cell images were captured using a ZEISS LSM 710 confocal microscope with a 20× objective lens. Image acquisition and processing were carried out using ZEN Microscopy Software (Zeiss), with standard settings applied for visualization.

Immunoprecipitation

Cells were collected and lysed in 500 μl of IP lysis buffer [150 mM NaCl, 25 mM HEPES pH 7.4, 10% glycerol, 0.5% IGEPAL CA-630, and protease inhibitor cocktails (Roche)] for 1 hour on a rotator at 4°C. After centrifugation at 12,000*g* for 15 min, cell lysates were immunoprecipitated with 2 μg of anti-Caspase 8/p43/p18 mouse (Proteintech, 66093-1-Ig, clone 2B9H8) in 0.5 ml of lysis buffer overnight at 4°C. Twenty microliters of Protein G magnetic beads (Thermo Fisher Scientific, 13424229) was then added for an additional 3 hours at 4°C. The immunoprecipitates were then washed four times with IP lysis buffer and the immune complexes were boiled with loading buffer for 5 min and analyzed by SDS-PAGE.

Purification of endogenous ubiquitin conjugates

Ubiquitin conjugates were purified using GST-1×UBAubq. Thirty micrograms of GST-1×UBAubq proteins were prebound to 15 µl of GSH-Sepharose 4B beads per sample and incubated at 4°C on a rotor for 2 hours. Cells from a 10-cm dish at 90% confluency per sample were lysed with 500 µl of lysis buffer (20 mM sodium phosphate, pH 7.4, 1% IGEPAL CA-630, 2 mM EDTA, 1 mM DTT, 10 mM N-ethylmaleimide, and protease inhibitor cocktails), centrifuged and supernatants collected. Fifty microliters from each sample was taken as input. The remainder was incubated with GST-1×UBAubq-bound Sepharose beads at 4°C on a rotator overnight. The beads were washed four times with lysis buffer and heated at 100°C for 5 min with 40 µl of 1X loading buffer diluted in 1% SDS. Twenty microliters of each sample was loaded onto a gel and analyzed by immunoblot.

RNA isolation, cellular fractionation, and quantitative real-time PCR

Total RNA was extracted and purified using the purelink RNA mini kit (Fisher Scientific, 10307963) following the manufacturer's instructions. cDNA was synthesized by reverse transcription using the iScript™ cDNA synthesis kit (Bio-Rad, 1708891). Quantitative real-time PCR was performed using the SsoAdvanced universal SYBR® green supermix (Bio-Rad, 1725274) on a CFX Opus 384 real-time PCR system (Bio-Rad). Relative mRNA abundance was calculated by normalization to the indicated housekeeping genes. Where indicated, relative gene expression was further normalized to expression in the control group in the same experiment and represented as a fold change. More detailed information on the primers used is available in table S4.

Click chemistry labeling

For de novo protein labeling, cells grown to 80% confluence were washed three times with warm PBS and replaced with L-methionine-free media (Thermo Fisher Scientific, A1451701) methionine (Sigma-Aldrich, M5308) or L-azidohomoalanine (Merck Life Science, 900892) was then added to the media to a final concentration of 50 µM, followed by incubation for an additional 4 hours. Cells were washed twice with ice-cold PBS, harvested, and lysed in lysis buffer (1% NP-40 and 0.1% SDS in PBS). After centrifugation, the supernatants were collected. For a 200-µl reaction volume, 1 µl of Biotin-PEG4-Alkyne (4 mM stock solution) (Merck Life Science, 764213), 10 µl of THPTA (100 mM stock solution) (Merck Life Science, 762342), 4 µl of $CuSO_4$ (50 mM stock solution) (Jena Bioscience, CLK-MI004-50), and 10 µl of sodium ascorbate (300 mM stock solution) (Merck Life Science, A7631) were added and briefly vortexed to ensure thorough mixing. The mixture was added to 175 µl of cell lysates (prepared using 200 µl of lysis buffer per well of a six-well plate) and continuously vortexed for 2 hours at room temperature. The 200-µl reaction was then diluted with 800 µl of 0.1% SDS in PBS and desalted using a PD10 Column (GE Healthcare, GE17-0851-01) according to the manufacturer's instructions. The 3.5-ml desalted solution was purified by incubation with 25 µl of Pierce™ streptavidin magnetic beads (Thermo Fisher Scientific, 88817) at 4°C overnight. The beads were washed three times with 0.1% SDS in PBS and eluted by heating at 100°C for 5 min with 60 µl of 1X loading buffer diluted with 1% SDS. Finally, 10 µl of each sample was loaded onto a gel for detection by immunoblotting.

Bioinformatics analysis

Ribo-seq data for detection of initiation sites from datasets GSE87328, GSE131650, GSE58207, GSE65885, SRA160745, GSE94460, GSE74279, and GSE75290 were analyzed using the GWIPS-viz Genome Browser (*56*). Ribosome profiling data GSE69906 and GSE74139 were downloaded and visualized by Integrative Genomics Viewer (IGV). DNA sequence conservation across species was analyzed using the UCSC Genome Browser

Quantification and statistical analysis

Error bars represent the standard error of the mean. Statistical analyses were performed using GraphPad Prism 10 software. Statistical parameters, *P* values, and methods are mentioned within the figures and legends. Briefly, when comparing two datasets, an F-test was first used to test the variance of the datasets and then a t-test was used to calculate the *P* values using assumptions of homoscedasticity or heteroscedasticity accordingly. Normal distribution and variance similarity were assessed with the D'Agostino and Pearson omnibus normality test. For comparison of more than two groups, one-way ANOVA or two-way ANOVA with respective corrections was used. Where indicated, experiments were repeated at least three times. No exclusion criteria were pre-established. All collected samples were included in the analysis, with no data excluded. Investigators were not blinded to allocation during experiments and outcome assessment.

Supplementary Materials

Materials and Methods

Fig. S1 to S12

Tables S1 to S4

Data files S1 to S4

MDAR Reproducibility Checklist

REFERENCES AND NOTES

1. D. C. Angus, T. van der Poll, Severe sepsis and septic shock. *N Engl J Med* **369**, 840–851 (2013).
2. M. Hrdinka, M. Gyrd-Hansen, The Met1-Linked Ubiquitin Machinery: Emerging Themes of (De)regulation. *Mol Cell* **68**, 265–280 (2017).
3. O. Takeuchi, S. Akira, Pattern recognition receptors and inflammation. *Cell* **140**, 805–820 (2010).
4. D. Siegmund, H. Wajant, TNF and TNF receptors as therapeutic targets for rheumatic diseases and beyond. *Nature reviews. Rheumatology* **19**, 576–591 (2023).
5. N. Peltzer, H. Walczak, Cell Death and Inflammation - A Vital but Dangerous Liaison. *Trends in immunology* **40**, 387–402 (2019).
6. G. van Loo, M. J. M. Bertrand, Death by TNF: a road to inflammation. *Nat Rev Immunol* **23**, 289–303 (2023).
7. G. D. Kalliolias, L. B. Ivashkiv, TNF biology, pathogenic mechanisms and emerging therapeutic strategies. *Nature reviews. Rheumatology* **12**, 49–62 (2016).
8. R. Medzhitov, D. S. Schneider, M. P. Soares, Disease tolerance as a defense strategy. *Science* **335**, 936–941 (2012).
9. A. Krikos, C. D. Laherty, V. M. Dixit, Transcriptional activation of the tumor necrosis factor alpha-inducible zinc finger protein, A20, is mediated by kappa B elements. *J Biol Chem* **267**, 17971–17976 (1992).
10. O. Le Bail, R. Schmidt-Ullrich, A. Israel, Promoter analysis of the gene encoding the I kappa B-alpha/MAD3 inhibitor of NF-kappa B: positive regulation by members of the rel/NF-kappa B family. *EMBO J* **12**, 5043–5049 (1993).
11. E. G. Lee, D. L. Boone, S. Chai, S. L. Libby, M. Chien, J. P. Lodolce, A. Ma, Failure to regulate TNF-induced NF-kappaB and cell death responses in A20-deficient mice. *Science* **289**, 2350–2354 (2000).
12. N. R. Rice, M. K. Ernst, In vivo control of NF-kappa B activation by I kappa B alpha. *EMBO J* **12**, 4685–4695 (1993).
13. S. Xanthoulea, M. Pasparakis, S. Kousteni, C. Brakebusch, D. Wallach, J. Bauer, H. Lassmann, G. Kollias, Tumor necrosis factor (TNF) receptor shedding controls thresholds of innate immune activation that balance opposing TNF functions in infectious and inflammatory diseases. *The Journal of experimental medicine* **200**, 367–376 (2004).
14. C. Cudrici, N. Deuitch, I. Aksentijevich, Revisiting TNF Receptor-Associated Periodic Syndrome (TRAPS): Current Perspectives. *Int J Mol Sci* **21**, (2020).
15. A. M. Michel, A. M. Ahern, C. A. Donohue, P. V. Baranov, GWIPS-viz as a tool for exploring ribosome profiling evidence supporting the synthesis of alternative proteoforms. *Proteomics* **15**, 2410–2416 (2015).
16. Z. Ji, R. Song, A. Regev, K. Struhl, Many lncRNAs, 5'UTRs, and pseudogenes are translated and some are likely to express functional proteins. *eLife* **4**, e08890 (2015).
17. J. Crappe, E. Ndah, A. Koch, S. Steyaert, D. Gawron, S. De Keulenaer, E. De Meester, T. De Meyer, W. Van Criekinge, P. Van Damme, G. Menschaert, PROTEOFORMER: deep proteome coverage through ribosome profiling and MS integration. *Nucleic Acids Res* **43**, e29 (2015).
18. X. Gao, J. Wan, B. Liu, M. Ma, B. Shen, S. B. Qian, Quantitative profiling of initiating ribosomes in vivo. *Nature methods* **12**, 147–153 (2015).

19. D. Gawron, E. Ndah, K. Gevaert, P. Van Damme, Positional proteomics reveals differences in N-terminal proteoform stability. *Molecular systems biology* **12**, 858 (2016).

20. D. Fijalkowska, S. Verbruggen, E. Ndah, V. Jonckheere, G. Menschaert, P. Van Damme, eIF1 modulates the recognition of suboptimal translation initiation sites and steers gene expression via uORFs. *Nucleic Acids Res* **45**, 7997–8013 (2017).

21. P. Zhang, D. He, Y. Xu, J. Hou, B. F. Pan, Y. Wang, T. Liu, C. M. Davis, E. A. Ehli, L. Tan, F. Zhou, J. Hu, Y. Yu, X. Chen, T. M. Nguyen, J. M. Rosen, D. H. Hawke, Z. Ji, Y. Chen, Genome-wide identification and differential analysis of translational initiation. *Nature communications* **8**, 1749 (2017).

22. J. Chen, A. D. Brunner, J. Z. Cogan, J. K. Nunez, A. P. Fields, B. Adamson, D. N. Itzhak, J. Y. Li, M. Mann, M. D. Leonetti, J. S. Weissman, Pervasive functional translation of noncanonical human open reading frames. *Science* **367**, 1140–1146 (2020).

23. A. Raj, S. H. Wang, H. Shim, A. Harpak, Y. I. Li, B. Engelmann, M. Stephens, Y. Gilad, J. K. Pritchard, Thousands of novel translated open reading frames in humans inferred by ribosome footprint profiling. *eLife* **5**, (2016).

24. B. G. Luukkonen, W. Tan, S. Schwartz, Efficiency of reinitiation of translation on human immunodeficiency virus type 1 mRNAs is determined by the length of the upstream open reading frame and by intercistronic distance. *Journal of virology* **69**, 4086–4094 (1995).

25. J. Huyghe, D. Priem, M. J. M. Bertrand, Cell death checkpoints in the TNF pathway. *Trends in immunology* **44**, 628–643 (2023).

26. J. Huyghe, D. Priem, L. Van Hove, B. Gilbert, J. Fritsch, Y. Uchiyama, E. Hoste, G. van Loo, M. J. M. Bertrand, ATG9A prevents TNF cytotoxicity by an unconventional lysosomal targeting pathway. *Science* **378**, 1201–1207 (2022).

27. J. A. Rickard, H. Anderton, N. Etemadi, U. Nachbur, M. Darding, N. Peltzer, N. Lalaoui, K. E. Lawlor, H. Vanyai, C. Hall, A. Bankovacki, L. Gangoda, W. W. Wong, J. Corbin, C. Huang, E. S. Mocarski, J. M. Murphy, W. S. Alexander, A. K. Voss, D. L. Vaux, W. J. Kaiser, H. Walczak, J. Silke, TNFR1-dependent cell death drives inflammation in Sharpin-deficient mice. *eLife* **3**, (2014).

28. C. Yang, J. Li, L. Yu, Z. Zhang, F. Xu, L. Jiang, X. Zhou, S. He, Regulation of RIP3 by the transcription factor Sp1 and the epigenetic regulator UHRF1 modulates cancer cell necroptosis. *Cell death & disease* **8**, e3084 (2017).

29. L. Duprez, N. Takahashi, F. Van Hauwermeiren, B. Vandendriessche, V. Goossens, T. Vanden Berghe, W. Declercq, C. Libert, A. Cauwels, P. Vandenabeele, RIP kinase-dependent necrosis drives lethal systemic inflammatory response syndrome. *Immunity* **35**, 908–918 (2011).

30. R. Karki, B. R. Sharma, S. Tuladhar, E. P. Williams, L. Zalduondo, P. Samir, M. Zheng, B. Sundaram, B. Banoth, R. K. S. Malireddi, P. Schreiner, G. Neale, P. Vogel, R. Webby, C. B. Jonsson, T. D. Kanneganti, Synergism of TNF-alpha and IFN-gamma Triggers Inflammatory Cell Death, Tissue Damage, and Mortality in SARS-CoV-2 Infection and Cytokine Shock Syndromes. *Cell* **184**, 149–168 e117 (2021).

31. L. Vereecke, M. Sze, C. Mc Guire, B. Rogiers, Y. Chu, M. Schmidt-Supprian, M. Pasparakis, R. Beyaert, G. van Loo, Enterocyte-specific A20 deficiency sensitizes to tumor necrosis factor-induced toxicity and experimental colitis. *The Journal of experimental medicine* **207**, 1513–1523 (2010).

32. D. Lena, P. Kalfon, J. C. Preiser, C. Ichai, Glycemic control in the intensive care unit and during the postoperative period. *Anesthesiology* **114**, 438–444 (2011).

33. K. Pfeffer, T. Matsuyama, T. M. Kundig, A. Wakeham, K. Kishihara, A. Shahinian, K. Wiegmann, P. S. Ohashi, M. Kronke, T. W. Mak, Mice deficient for the 55 kd tumor necrosis factor receptor are resistant to endotoxic shock, yet succumb to L. monocytogenes infection. *Cell* **73**, 457–467 (1993).

34. Y. Shikama, T. Kuroishi, Y. Nagai, Y. Iwakura, H. Shimauchi, H. Takada, S. Sugawara, Y. Endo, Muramyldipeptide augments the actions of lipopolysaccharide in mice by stimulating macrophages to produce pro-IL-1beta and by down-regulation of the suppressor of cytokine signaling 1 (SOCS1). *Innate immunity* **17**, 3–15 (2011).

35. M. J. Landrum, J. M. Lee, M. Benson, G. R. Brown, C. Chao, S. Chitipiralla, B. Gu, J. Hart, D. Hoffman, W. Jang, K. Karapetyan, K. Katz, C. Liu, Z. Maddipatla, A. Malheiro, K. McDaniel, M. Ovetsky, G. Riley, G. Zhou, J. B. Holmes, B. L. Kattman, D. R. Maglott, ClinVar: improving access to variant interpretations and supporting evidence. *Nucleic acids research* **46**, D1062–D1067 (2018).

36. S. Siebert, N. Amos, C. A. Fielding, E. C. Wang, I. Aksentijevich, B. D. Williams, P. Brennan, Reduced tumor necrosis factor signaling in primary human fibroblasts containing a tumor necrosis factor receptor superfamily 1A mutant. *Arthritis Rheum* **52**, 1287–1292 (2005).

37. T. Akagi, S. Hiramatsu-Asano, K. Ikeda, H. Hirano, S. Tsuji, A. Yahagi, M. Iseki, M. Matsuyama, T. W. Mak, K. Nakano, K. Ishihara, Y. Morita, T. Mukai, TRAPS mutations in Tnfrsf1a decrease the responsiveness to TNFalpha via reduced cell surface expression of TNFR1. *Front Immunol* **13**, 926175 (2022).

38. S. P. Chothani, E. Adami, A. A. Widjaja, S. R. Langley, S. Viswanathan, C. J. Pua, N. T. Zhihao, N. Harmston, G. D'Agostino, N. Whiffin, W. Mao, J. F. Ouyang, W. W. Lim, S. Lim, C. Q. E. Lee, A. Grubman, J. Chen, J. P. Kovalik, K. Tryggvason, J. M. Polo, L. Ho, S. A. Cook, O. J. L. Rackham, S. Schafer, A high-resolution map of human RNA translation. *Mol Cell* **82**, 2885–2899 e2888 (2022).

39. M. Koritzinsky, M. G. Magagnin, T. van den Beucken, R. Seigneuric, K. Savelkouls, J. Dostie, S. Pyronnet, R. J. Kaufman, S. A. Weppler, J. W. Voncken, P. Lambin, C. Koumenis, N. Sonenberg, B. G. Wouters, Gene expression during acute and prolonged hypoxia is regulated by distinct mechanisms of translational control. *EMBO J* **25**, 1114–1125 (2006).

40. A. Romero-Ruiz, L. Bautista, V. Navarro, A. Heras-Garvin, R. March-Diaz, A. Castellano, R. Gomez-Diaz, M. J. Castro, E. Berra, J. Lopez-Barneo, A. Pascual, Prolyl hydroxylase-dependent modulation of eukaryotic elongation factor 2 activity and protein translation under acute hypoxia. *J Biol Chem* **287**, 9651–9658 (2012).

41. L. Samluk, M. Urbanska, K. Kisielewska, K. Mohanraj, M. J. Kim, K. Machnicka, E. Liszewska, J. Jaworski, A. Chacinska, Cytosolic translational responses differ under conditions of severe short-term and long-term mitochondrial stress. *Mol Biol Cell* **30**, 1864–1877 (2019).

42. A. C. Vind, G. Snieckute, M. Blasius, C. Tiedje, N. Krogh, D. B. Bekker-Jensen, K. L. Andersen, C. Nordgaard, M. A. X. Tollenaere, A. H. Lund, J. V. Olsen, H. Nielsen, S. Bekker-Jensen, ZAKalpha Recognizes Stalled Ribosomes through Partially Redundant Sensor Domains. *Mol Cell* **78**, 700–713 e707 (2020).

43. C. T. Taylor, S. P. Colgan, Regulation of immunity and inflammation by hypoxia in immunological niches. *Nat Rev Immunol* **17**, 774–785 (2017).

44. K. Pakos-Zebrucka, I. Koryga, K. Mnich, M. Ljujic, A. Samali, A. M. Gorman, The integrated stress response. *EMBO Rep* **17**, 1374–1395 (2016).

45. E. Marlin, M. Valencia, N. Peregrin, R. Ferrero, M. J. Nicolas, R. Vinueza-Gavilanes, A. Pineda-Lucena, J. Artieda, M. Arrasate, T. Aragon, Pharmacological inhibition of the integrated stress response accelerates disease progression in an amyotrophic lateral sclerosis mouse model. *Br J Pharmacol* **181**, 495–508 (2024).

46. O. Tirosh, Y. Cohen, A. Shitrit, O. Shani, V. T. Le-Trilling, M. Trilling, G. Friedlander, M. Tanenbaum, N. Stern-Ginossar, The Transcription and Translation Landscapes during Human Cytomegalovirus Infection Reveal Novel Host-Pathogen Interactions. *PLoS pathogens* **11**, e1005288 (2015).

47. A. P. Fields, E. H. Rodriguez, M. Jovanovic, N. Stern-Ginossar, B. J. Haas, P. Mertins, R. Raychowdhury, N. Hacohen, S. A. Carr, N. T. Ingolia, A. Regev, J. S. Weissman, A Regression-Based Analysis of Ribosome-Profiling Data Reveals a Conserved Complexity to Mammalian Translation. *Molecular cell* **60**, 816–827 (2015).

48. S. I. Grivennikov, A. V. Tumanov, D. J. Liepinsh, A. A. Kruglov, B. I. Marakusha, A. N. Shakhov, T. Murakami, L. N. Drutskaya, I. Forster, B. E. Clausen, L. Tessarollo, B. Ryffel, D. V. Kuprash, S. A. Nedospasov, Distinct and nonredundant in vivo functions of TNF produced by t cells and macrophages/neutrophils: protective and deleterious effects. *Immunity* **22**, 93–104 (2005).

49. D. Kontoyiannis, M. Pasparakis, T. T. Pizarro, F. Cominelli, G. Kollias, Impaired on/off regulation of TNF biosynthesis in mice lacking TNF AU-rich elements: implications for joint and gut-associated immunopathologies. *Immunity* **10**, 387–398 (1999).

50. A. Thiran, I. Petta, G. Blancke, M. Thorp, G. Planckaert, M. Jans, V. Andries, K. Barbry, E. Gilis, J. Coudenys, T. Hochepied, C. Vanhove, E. Gracey, E. Dumas, T. Manuelo, I. Josipovic, G. van Loo, D. Elewaut, L. Vereecke, Sterile triggers drive joint inflammation in TNF- and IL-1beta-dependent mouse arthritis models. *EMBO Mol Med* **15**, e17691 (2023).

51. T. E. Dever, I. P. Ivanov, A. G. Hinnebusch, Translational regulation by uORFs and start codon selection stringency. *Genes & development* **37**, 474–489 (2023).

52. J. Zhou, J. Wan, X. E. Shu, Y. Mao, X. M. Liu, X. Yuan, X. Zhang, M. E. Hess, J. C. Bruning, S. B. Qian, N(6)-Methyladenosine Guides mRNA Alternative Translation during Integrated Stress Response. *Mol Cell* **69**, 636–647 e637 (2018).

53. T. E. Dever, I. P. Ivanov, A. G. Hinnebusch, Translational regulation by uORFs and start codon selection stringency. *Genes & development* **37**, 474–489 (2023).

54. M. Hrdinka, B. K. Fiil, M. Zucca, D. Leske, K. Bagola, M. Yabal, P. R. Elliott, R. B. Damgaard, D. Komander, P. J. Jost, M. Gyrd-Hansen, CYLD Limits Lys63- and Met1-Linked Ubiquitin at Receptor Complexes to Regulate Innate Immune Signaling. *Cell reports* **14**, 2846–2858 (2016).

55. R. Y. Tsien, The green fluorescent protein. *Annu Rev Biochem* **67**, 509–544 (1998).

56. A. M. Michel, S. J. Kiniry, P. B. F. O'Connor, J. P. Mullan, P. V. Baranov, GWIPS-viz: 2018 update. *Nucleic Acids Res* **46**, D823–D830 (2018).

Acknowledgements: We thank N. Masson and P.J. Ratcliffe (University of Oxford) for advice on hypoxia and for sharing equipment, C. Chuang and M. Davies (University of Copenhagen) for access to hypoxia station, and S. Bekker-Jensen (University of Copenhagen) for advice and access to UVB irradiation equipment. We thank C. Goding (University of Oxford) and S. Kriaucionis (University of Oxford) for reading iterations of the manuscript and members of the M.G-H. group for helpful advice and suggestions. We acknowledge the contribution to this study made by the Core Facility for Transgenic Animals, the Animal Housing and Breeding Facility at the Department of Experimental Medicine, the Flow Cytometry and Single Cell Core Facility, and the Histology Facility (University of Copenhagen). We thank John Radcliffe Hospital in Oxford and the patients who provided duodenal biopsies. We thank BioRender.com for providing elements in the schematic figures.

Funding: This work was supported by the Ludwig Institute for Cancer Research Ltd (University of Oxford) and the LEO foundation (University of Copenhagen, grant number LF18500). Work in the M.G-H. lab was supported by a Wellcome Trust Fellowship (102894/Z/13/Z and 215612/Z/19/Z) and the Novo Nordisk Foundation (NNF200C0059392). C.S.K.L. was supported by a fellowship from Swiss National Science Foundation (P300P3_155374). B.M. was supported by CRUK (CRUK-OC-DPhil17-BM).

Author contributions: Conceptualization: B.M. and M.G-H. Data curation: B.M. Formal analysis: B.M. Funding acquisition: M.G-H. and B.M. Investigation: B.M. Methodology: B.M., W.L., J.R., X.Y.H., M.K., V.P.A., M.S., M.J., C.S.K..L, and B.V.D.E. Resources: X.L. Supervision: M.G-H. Visualization: B.M. and M.G-H. Writing—original draft: B.M. and M.G-H. Writing—review and editing: B.M. and M.G-H.

Declaration of interests: Authors declare that they have no competing interests.

Data, code, and materials availability: Uncropped immunoblots are provided in data file S3 and tabulated raw data underlying the figures are provided in data file S4. All data needed to evaluate the conclusions are available in the main text or the supplementary materials.

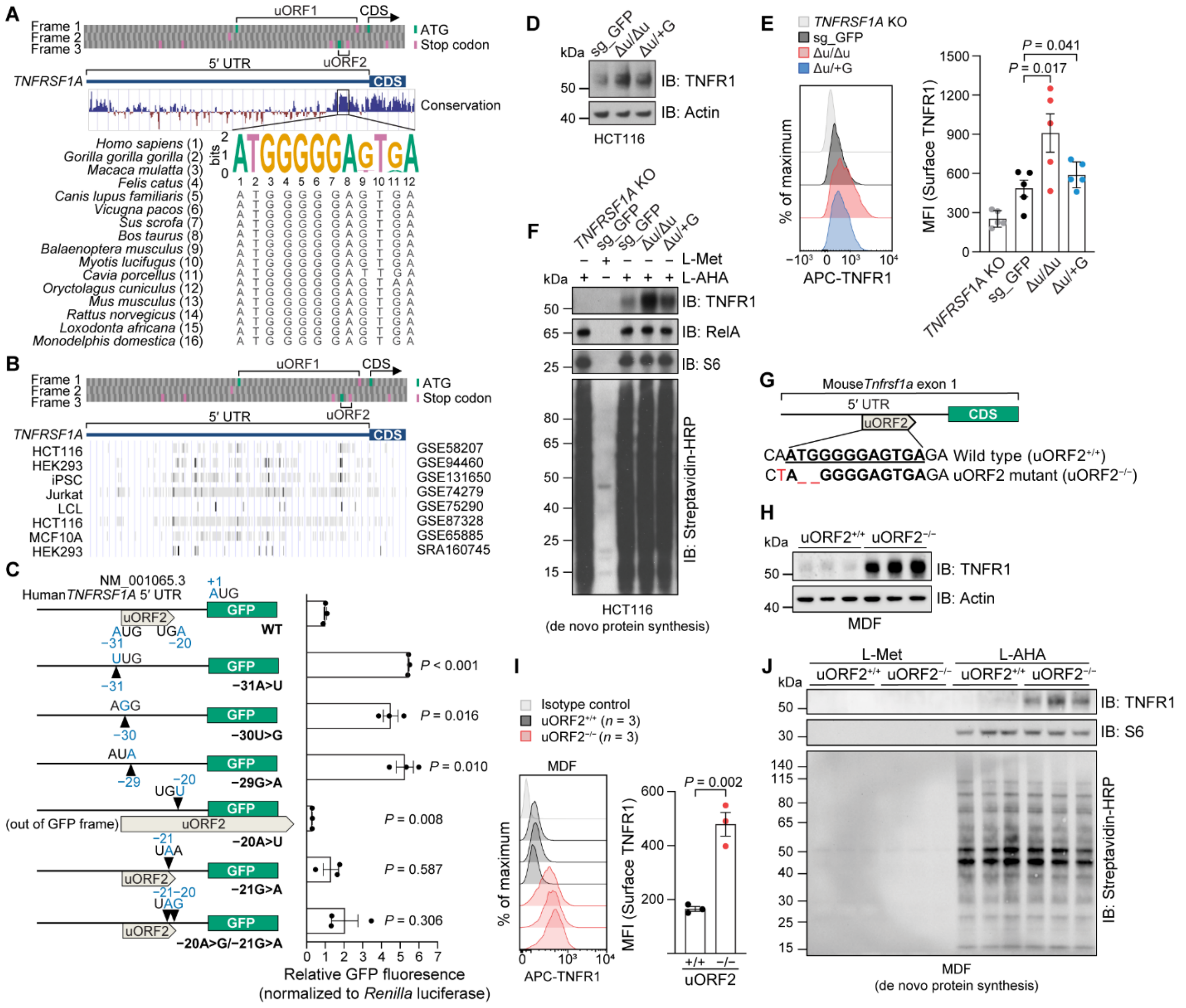

Fig. 1. uORF2 restricts TNFR1 translation in human and mouse cells. (**A**) Evolutionary conservation of *TNFRSF1A* uORF2 across species. (**B**) Ribo-seq analysis of ribosome initiation sites on the human *TNFRSF1A* transcript in the indicated cells, based on referenced studies. (**C**) Schematic of human *TNFRSF1A* 5′ UTR-GFP reporter constructs, with GFP levels shown to the right. GFP levels were measured by fluorescence and normalized to *Renilla* luciferase and are presented as fold changes relative to WT control. (**D**) Total TNFR1 protein levels in HCT116 WT (sg_GFP) and uORF2 mutant clones (Δu/Δu, Δu/+G), analyzed by immunoblotting. (**E**) Surface TNFR1 in HCT116 WT, uORF2 mutant clones, and *TNFRSF1A* knockout cells, measured by flow cytometry with anti-TNFR1 antibody staining. (**F**) Newly synthesized biotinylated proteins were purified via streptavidin beads and analyzed by immunoblotting. HCT116 WT and uORF2 mutant clones were incubated with 50 μM L-methionine (L-Met) or L-Azidohomoalanine (L-AHA) for 4 hours. (**G**) Schematic illustration of the mutation introduced in exon 1 of the mouse *Tnfrsf1a* gene.

(**H** and **I**) The (H) total and (I) surface TNFR1 protein levels in primary MDFs from uORF2$^{+/+}$ and uORF2$^{-/-}$ mice. (**J**) De novo–synthesized biotin-labeled proteins were purified via streptavidin beads and analyzed by immunoblotting. Primary MDFs from uORF2$^{+/+}$ and uORF2$^{-/-}$ mice treated with 50 μM L-Met or L-AHA for 4 hours. Data are presented as means ± SEM of [(C) and (E)] at least three independent experiments, [(D) and (F)] one representative experiment of three independent experiments with similar results, and [(H) to (J)] one experiment with three biological replicates. [(C), (E), and (I)] Statistical significance was determined by one-way ANOVA with Bonferroni's correction.

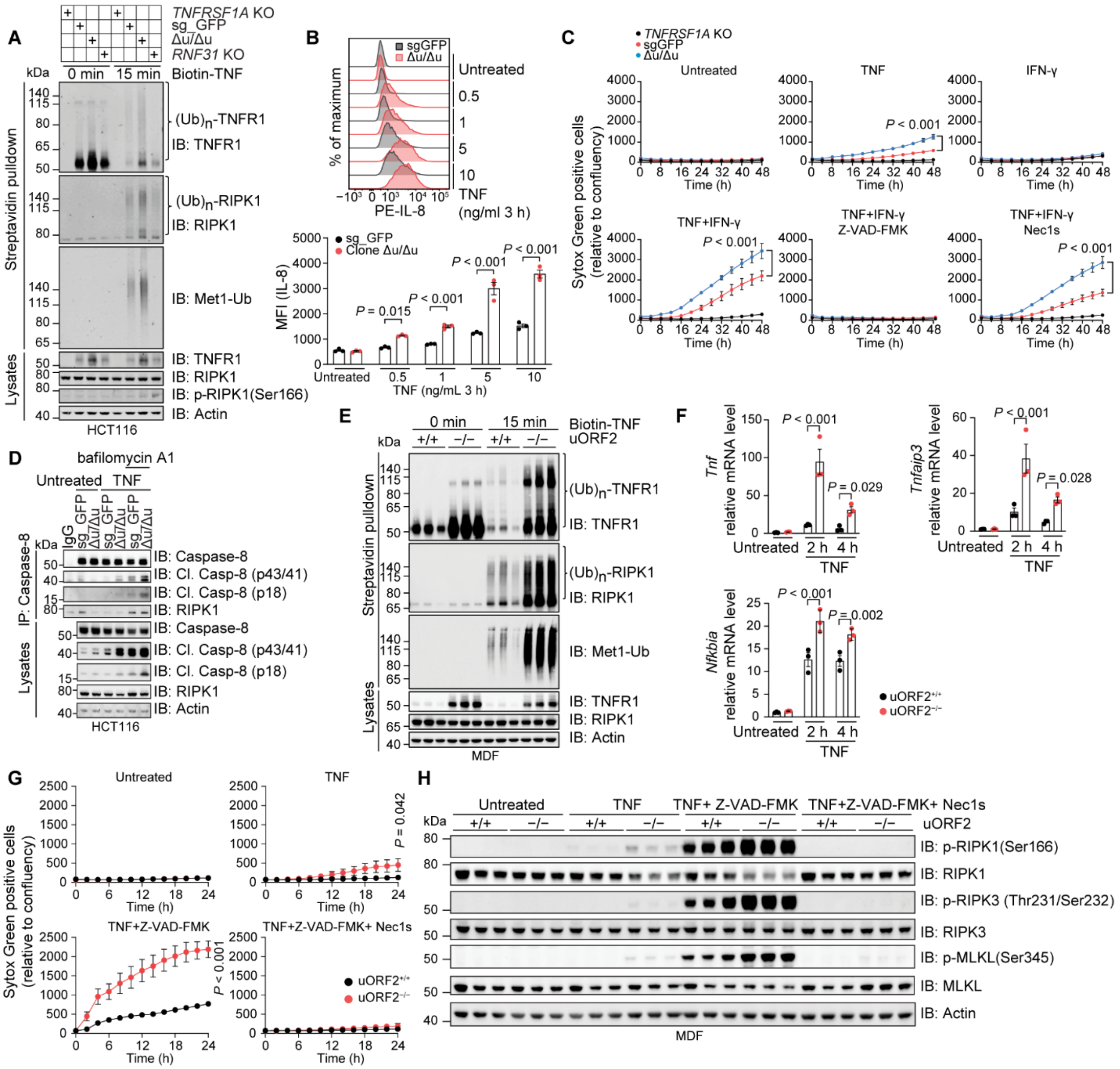

Fig. 2. TNFR1 abundance is rate-limiting for TNF signaling and cell death. (**A**) TNFR1 complexes were purified using streptavidin beads and analyzed by immunoblotting. Cells were stimulated with 50 ng/ml of biotin-TNF for 15 min; for 0 min controls, biotin-TNF was added post-lysis. (**B**) Intracellular IL-8 was measured by flow cytometry and quantified. WT and uORF2-mutant HCT116 cells were treated with monensin for 1 hour, followed by treatment with the indicated concentration of TNF for 3 hours. (**C**) Cell death was monitored using Sytox Green and normalized to confluence. WT, uORF2-mutant, and *TNFRSF1A*-knockout HCT116 cells were treated with DMSO, 10 μM Z-VAD-FMK, or 10 μM Z-VAD-FMK plus 10 μM Nec1s for 1 hour, followed by 10 ng/ml of TNF, 10 ng/ml of IFN-γ, or both for 48 hours. (**D**) Caspase-8 complexes

were immunoprecipitated and immunoblotted. WT and uORF2-mutant HCT116 cells were stimulated with 10 ng/ml of TNF for 8 hours with or without 200 nM bafilomycin A1. (**E**) Pulled-down complexes were immunoblotted. WT and uORF2-mutant MDFs were stimulated with biotin-TNF as in (A). (**F**) Primary MDFs were stimulated with 10 ng/ml of TNF for indicated times. *Tnf*, *Tnfaip3*, and *Nfkbia* mRNA levels were quantified by qRT-PCR (normalized to *Actb*). (**G**) Cell death was measured by Sytox Green, and positive cells were normalized to confluence. uORF2$^{+/+}$ and uORF2$^{-/-}$ MDFs were treated as in (C), then stimulated with 10 ng/ml of mouse TNF for 24 h. (**H**) Cells in (G) were collected 3 hours after TNF stimulation for immunoblotting. Data are presented as means ± SEM from [(B) and (C)] at least three independent experiments, [(A) and (D)] a representative of three independent experiments with similar results, and [(E) to (H)] one experiment with three biological replicates. [(B), (C), (F), and (G).] Statistical significance was determined using two-way ANOVA with Bonferroni's correction.

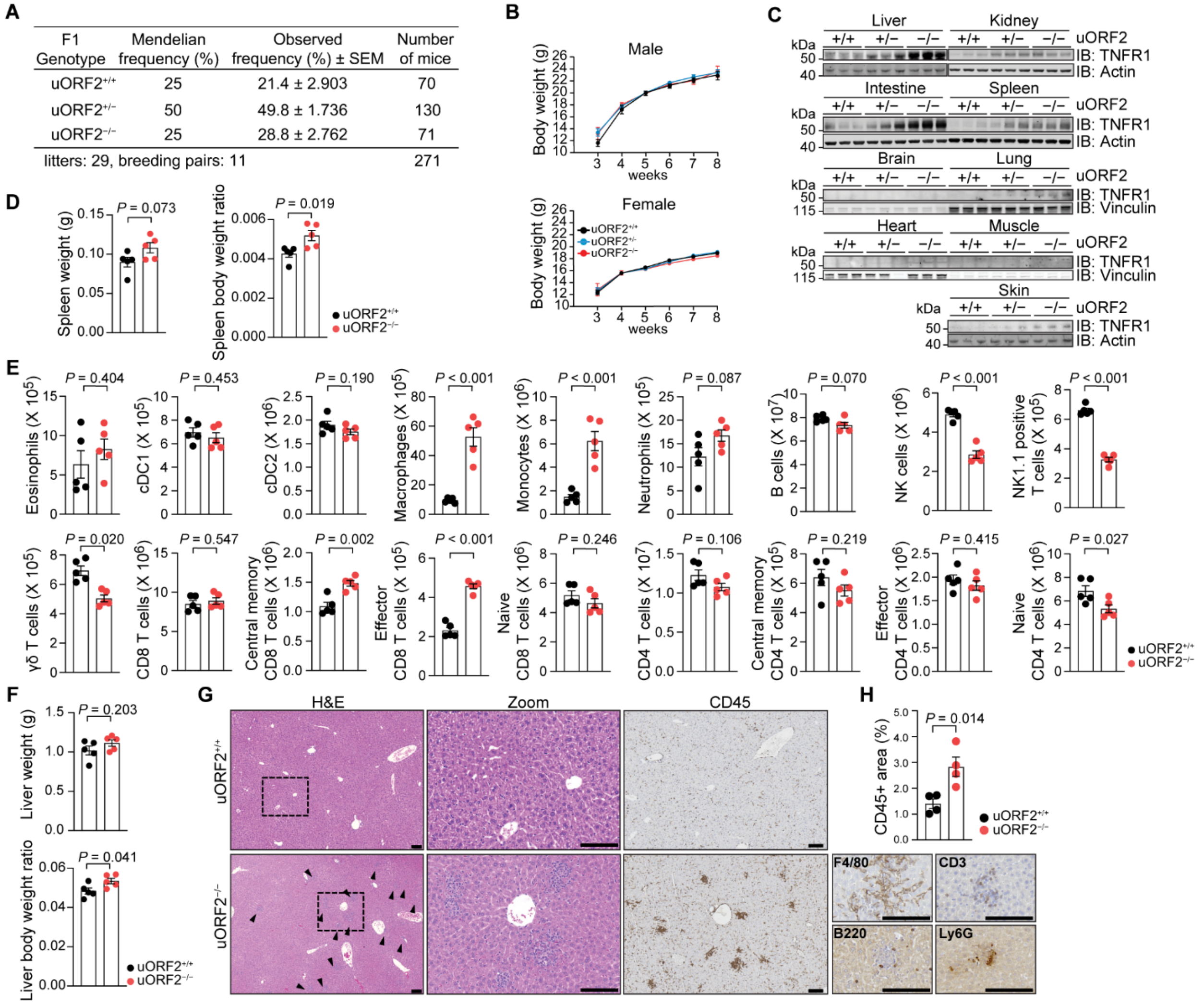

F1 Genotype	Mendelian frequency (%)	Observed frequency (%) ± SEM	Number of mice
$uORF2^{+/+}$	25	21.4 ± 2.903	70
$uORF2^{+/-}$	50	49.8 ± 1.736	130
$uORF2^{-/-}$	25	28.8 ± 2.762	71
litters: 29, breeding pairs: 11			271

Fig. 3. Disruption of *Tnfrsf1a* uORF2 causes immune dysregulation. (**A**) A table showing the expected and observed ratios of F1 mice with the indicated genotypes. (**B**) Growth curves of mice with the indicated genotypes. (**C**) Tissue lysates from WT and uORF2-mutant mice were analyzed by immunoblotting using the indicated antibodies. (**D**) Spleen weights and spleen-to-body weight ratios in WT and uORF2-mutant mice. (**E**) Immune landscape analysis in the spleen from WT and uORF2-mutant mice. (**F**) Liver weights and liver-to-body weight ratios in WT and uORF2-mutant mice. (**G**) Liver sections from WT and uORF2-mutant mice were stained with hematoxylin and eosin (H&E) and immunostained with the anti-CD45 antibodies. Liver sections from uORF2-mutant mice were further immunostained with anti-F4/80, anti-CD3, anti-B220 and anti-Ly6G antibodies. Arrows indicate immune cell aggregates. Scale bar: 100 μm. **(H)** Quantification of CD45+ areas from (G). Data are presented as the means ± SEM from (B) at least seven mice per time point, (C) one experiment with three mice per group, [(D), (E), and (F)] one experiment with

five mice per group, and [(G) and (H)] one representative of four mice with similar results. Statistical significance was determined by [(D) to (F), and (H)] unpaired two-tailed Student's *t* test.

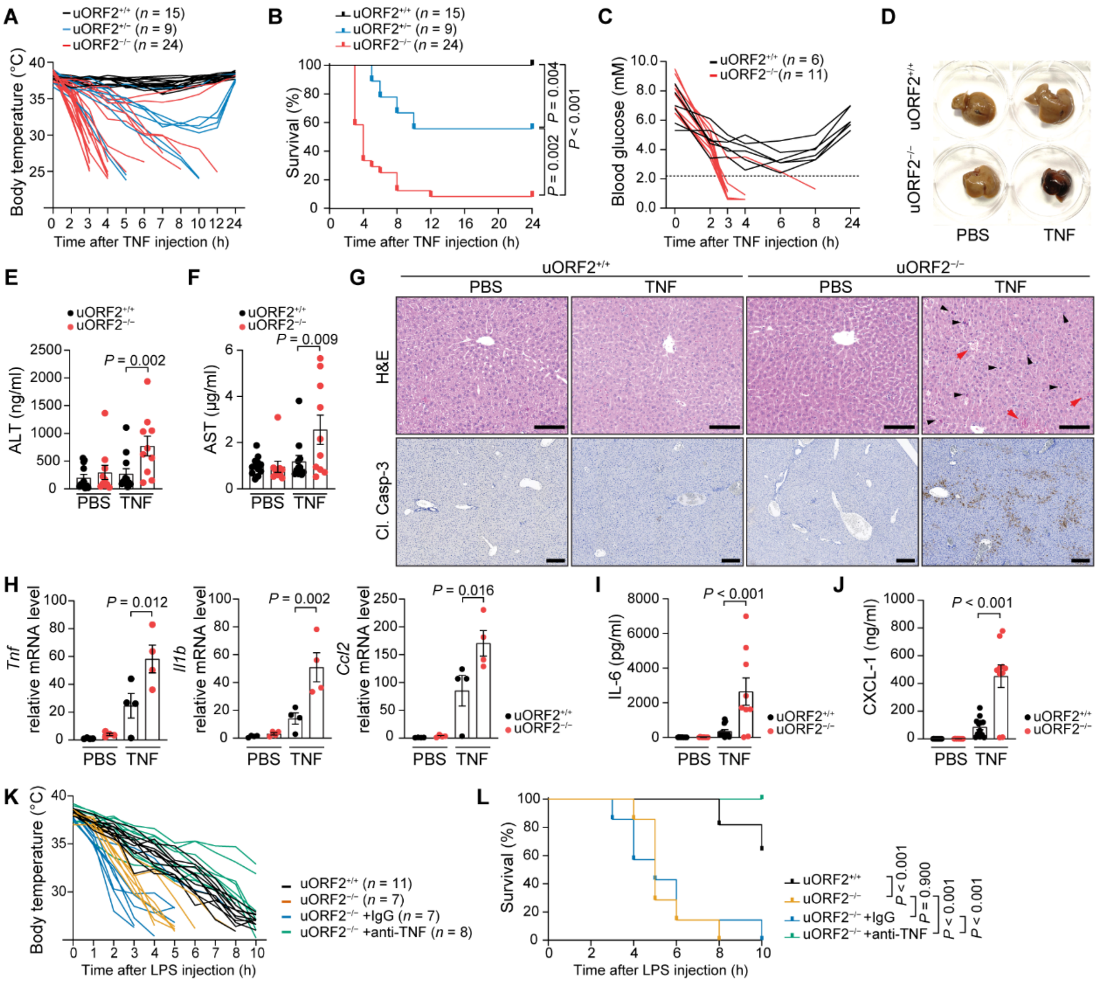

Fig. 4. *Tnfrsf1a* uORF2 promotes tissue tolerance to TNF. (**A** and **B**) uORF2$^{+/+}$, uORF2$^{+/-}$, and uORF2$^{-/-}$ mice received 250 μg per kilogram of body weight of recombinant mouse TNF. (A) Body temperature and (B) survival rate were monitored. (**C**) uORF2$^{+/+}$ and uORF2$^{-/-}$ mice received 250 μg per kilogram of body weight of recombinant mouse TNF. Blood glucose was then measured over time. Dashed line indicates severe hypoglycemia (2.2 mM). (**D**) Mice treated with 250 μg per kilogram of body weight of recombinant mouse TNF for 2 hours. Livers were shown. (**E** and **F**) Plasma from mice in (D) was analyzed for (E) ALT and (F) AST by ELISA. (**G**) Liver sections from (D) were stained with H&E and anti-cleaved caspase-3 antibody. Arrowheads: apoptotic hepatocytes. Arrows (red): vascular congestion areas. Scale bar: 100 μm. (**H**) *Tnf*, *Il1b*, and *Ccl2* mRNA levels in liver tissue from (D) were quantified by qRT-PCR and normalized to *Actb*. (**I** and **J**) Plasma from (D) was for (I) IL-6 and (J) CXCL-1 by ELISA. (**K** and **L**) Mice received MDP followed by LPS. Anti-TNF or isotype control antibodies were given 24 hours prior

to MDP. (K) Body temperature and (L) survival rate were monitored. 'n' indicates the number of mice used. Data are presented as the means ± SEM from [(A), (B), (C), (K), and (L)] combinations of at least two experiments with the indicated number of mice, [(D) and (G)] one representative of four mice with similar results, (H) one experiment with four mice per group, and [(E), (F), (I), and (J)] combinations of at least two experiments with a total of at least eight mice per group. Statistical significance was determined by [(B) and (L)] log-rank (Mantel–Cox) test, and [(E), (F), and (H) to (J)] two-way ANOVA with Bonferroni's correction.

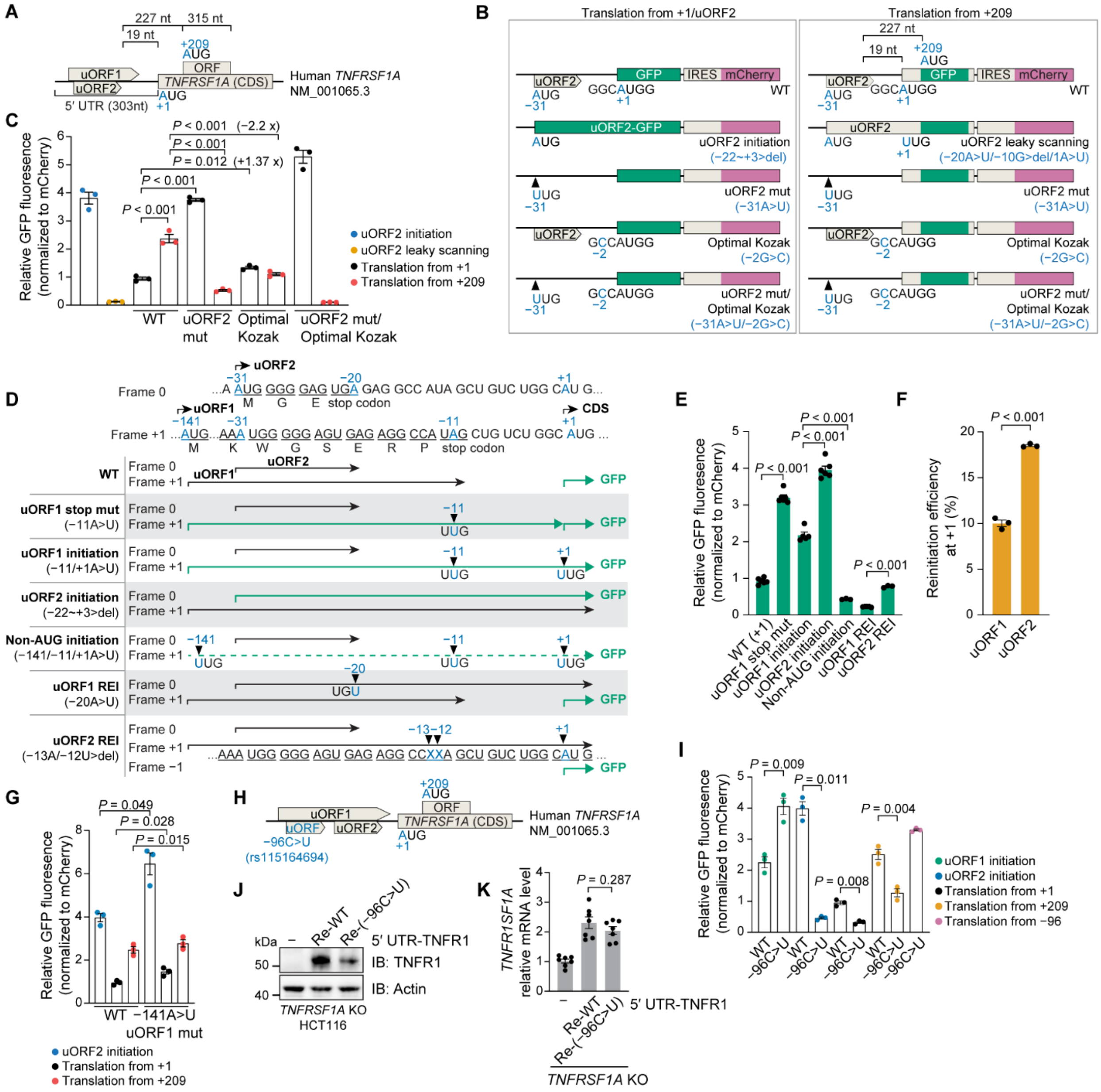

Fig. 5. Translation of uORF2 facilitates leaky scanning, reducing initiation at the *TNFRSF1A* start codon. (**A**) Schematic of the human *TNFRSF1A* mRNA (NM_001065.3) highlighting uORF1, uORF2, the internal ORF within the coding sequence, and the main coding sequence (CDS). (**B**) Design of 5′ UTR–GFP reporter constructs used to monitor translation from uORF2, the CDS start codon at +1, and a downstream ORF at +209 in WT and mutants. (**C**) HCT116 cells were transfected with the indicated reporters for 24 hours, GFP fluorescence was normalized to mCherry. (**D**) Reading-frame maps of the reporter variants. (**E** to **G**) Reporter analysis of uORF mutants. [(E) and (G)] GFP signals were normalized to mCherry. Reinitiation efficiency (F) is

shown as the ratio of GFP translated from the +1 start site to GFP initiated from the corresponding uORF. (**H**) Schematic of the neo-uORF created by the TRAPS-associated SNP rs115164694 (−96 C>T) within the *TNFRSF1A* 5′ UTR. (**I**) Effect of the −96 C>U neo-uORF on reporter output in HCT116 cells (24 hours post transfection, GFP normalized to mCherry). (**J** and **K**) *TNFRSF1A*-knockout HCT116 cells reconstituted with *TNFRSF1A* constructs bearing either the WT or −96 C>U 5′ UTR. (J) TNFR1 protein was analyzed by immunoblot and (K) mRNA abundance was quantified by qRT-PCR and normalized to *Actb*. Data are presented as means ± SEM [(C), (E), (F), (G), (I) and (K)] from at least three independent experiments and (J) representative data from five independent experiments with similar results. Statistical significance was determined by [(C), (E), (G), and (I)] one-way ANOVA with Bonferroni's correction, (K) Welch's ANOVA with dunnett's t3 correction, and (F) unpaired two-tailed Student's *t* test.

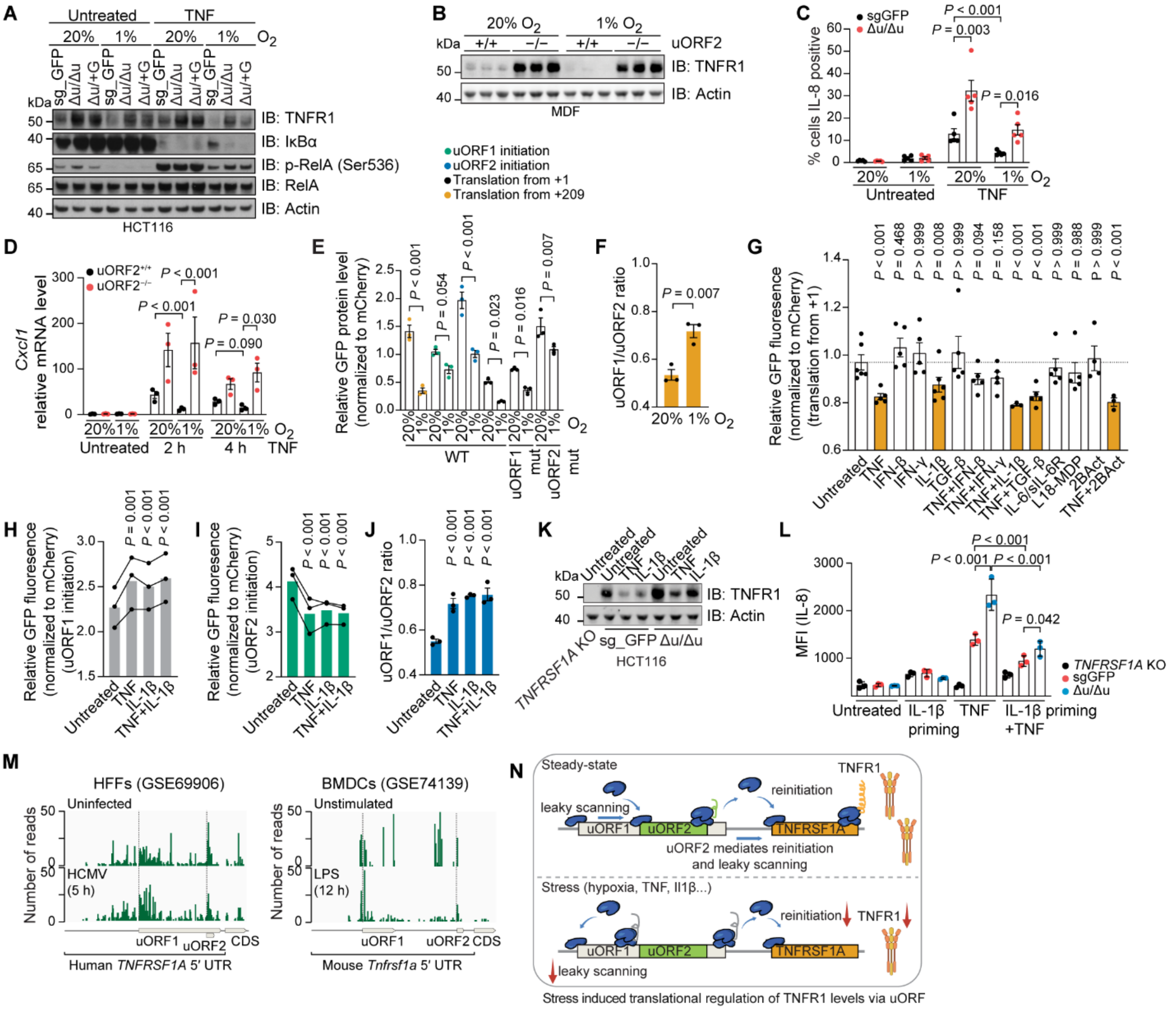

Fig. 6. Stress conditions increase uORF1 usage to suppress uORF2-mediated TNFR1 reinitiation. Immunoblotting of (**A**) HCT116 cells or (**B**) MDFs cultured under 20% or 1% oxygen for 24 hours or further stimulated with 10 ng/ml of TNF for 15 min. (**C**) Intracellular IL-8 was measured by flow cytometry. Cells were treated as in (A) for 20 hours, followed by stimulation with 10 ng/ml of TNF for 3 hours. (**D**) *Cxcl1* mRNA levels were quantified by qRT-PCR and normalized to *Actb*. MDFs were treated as in (A) for 20 hours, then stimulated with 10 ng/ml of TNF for the indicated times. (**E** to **J**) HCT116 cells transfected with the indicated reporters were treated as in (A), (E) translation from individual sites and (F) uORF1/uORF2 ratios were measured. Cells were also treated for 24 hours with the indicated stimuli (10 ng/ml each; 2BAct at 500 nM), translation from (G) +1, (H) uORF1, (I) uORF2, and (J) the uORF1/uORF2 ratio were determined. (**K**) Cells were treated with 10 ng/ml of TNF or 10 ng/ml of IL-1β for 24 hours and analyzed by immunoblot. (**L**) Intracellular IL-8 was measured by flow cytometry. Cells were pretreated with 10 ng/ml of IL-1β for 24 hours, then stimulated with 10 ng/ml of TNF for additional 3 hours. (**M**)

Ribosome occupancy at each uORF, ribosome-profiling data from HCMV-infected HFFs and LPS-treated BMDCs were quantified. (**N**) Schematic model of stress-induced uORF regulation. Data are presented as means ± SEM from [(C), (E) to (J), and (L)] at least three independent experiments, [(A) and (K)] representative data from three independent experiments with similar results, and [(B) and (D)] one experiment with three biological replicates. Statistical significance was determined by [(C), (D), and (L)] two-way ANOVA with Bonferroni's correction, [(E), (G) to (J)] one-way ANOVA with Bonferroni's correction, and (F) unpaired two-tailed Student's *t* test.

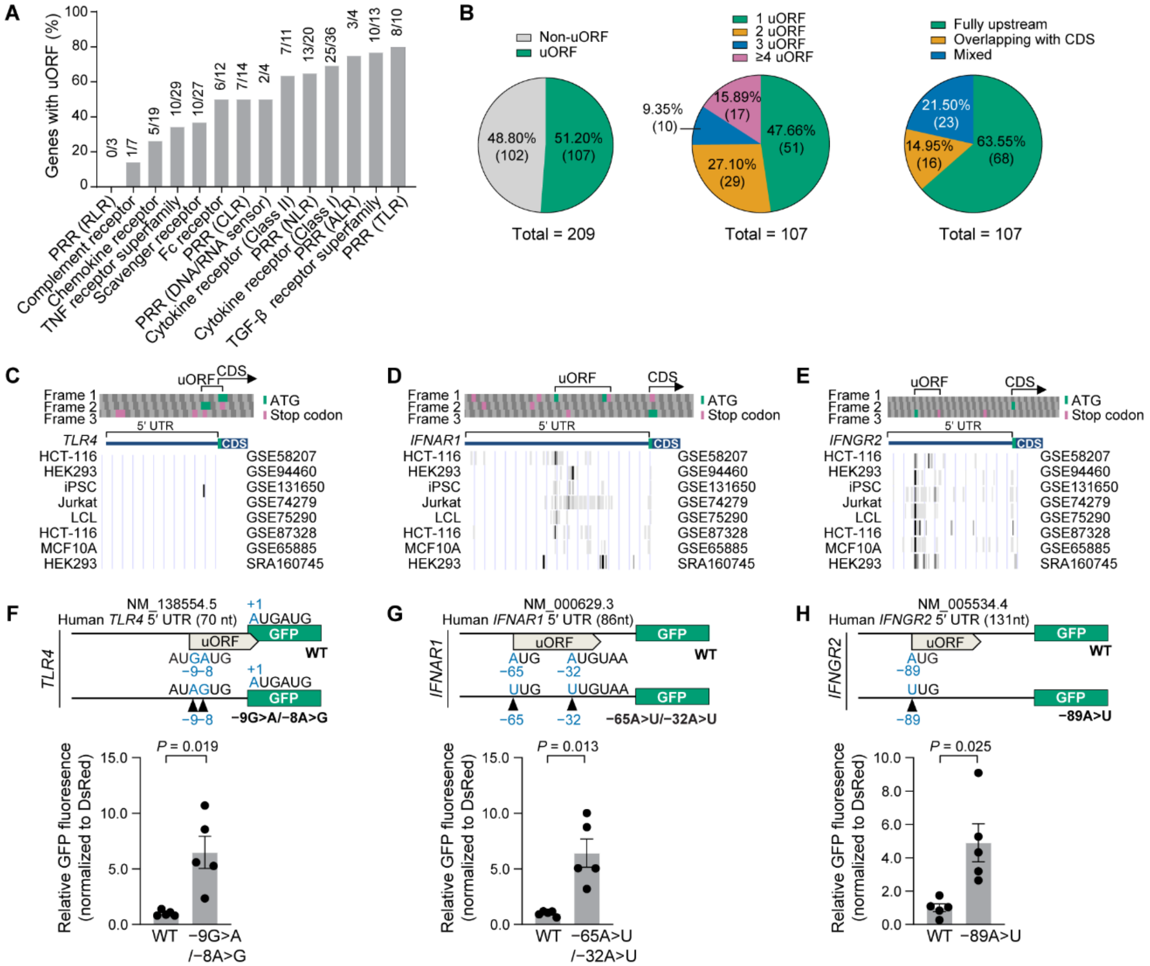

Fig. 7. uORFs act as negative regulators of translation for several immune receptors. (**A** and **B**) The canonical transcripts of immune-related receptor genes were analyzed. The percentage of genes containing uORFs is shown in (A), and the number and types of uORFs are shown in (B). (**C** to **E**) Initiating ribosome profiling data analysis of initiation sites for human (C) *TLR4*, (D) *IFNAR1*, and (E) *IFNGR2* in the indicated cells, based on referenced studies. (**F** to **H**) TOP: Schematic representation of GFP reporter constructs containing WT or uORF-mutant 5' UTRs from (F) *TLR4*, (G) *IFNAR1*, and (H) *IFNGR2*. Bottom: GFP and DsRed expression were analyzed by fluorescence. GFP fluorescence was normalized to DsRed. HCT116 cells were transfected with the indicated plasmid constructs along with an DsRed-expressing plasmid as a transfection control for 24 hours. Data are presented as means ± SEM from five independent experiments (F-H). Statistical significance was determined by (F-G) unpaired two-tailed Student's *t* test.

Supplementary Materials for

Upstream ORFs control TNFR1 abundance and tissue tolerance to TNF

Biao Ma, Wenxin Lyu, John Rizk, Xiaoyue Han, Majken Kjær, Vinnycius Pereira Almeida, Malin Jessen, Max Sauerland, Carol Sze Ki Leung, Benoit Van Den Eynde, Xin Lu, Mads Gyrd-Hansen

Corresponding author: Biao Ma, biao.ma@sund.ku.dk;
Mads Gyrd-Hansen, mgyrd@sund.ku.dk

The PDF file includes:

Figs. S1 to S12
Tables S1 to S4
Captions for data files S1 to S4

Other Supplementary Materials for this manuscript include the following:

Data files S1 to S4
MDAR Reproducibility Checklist

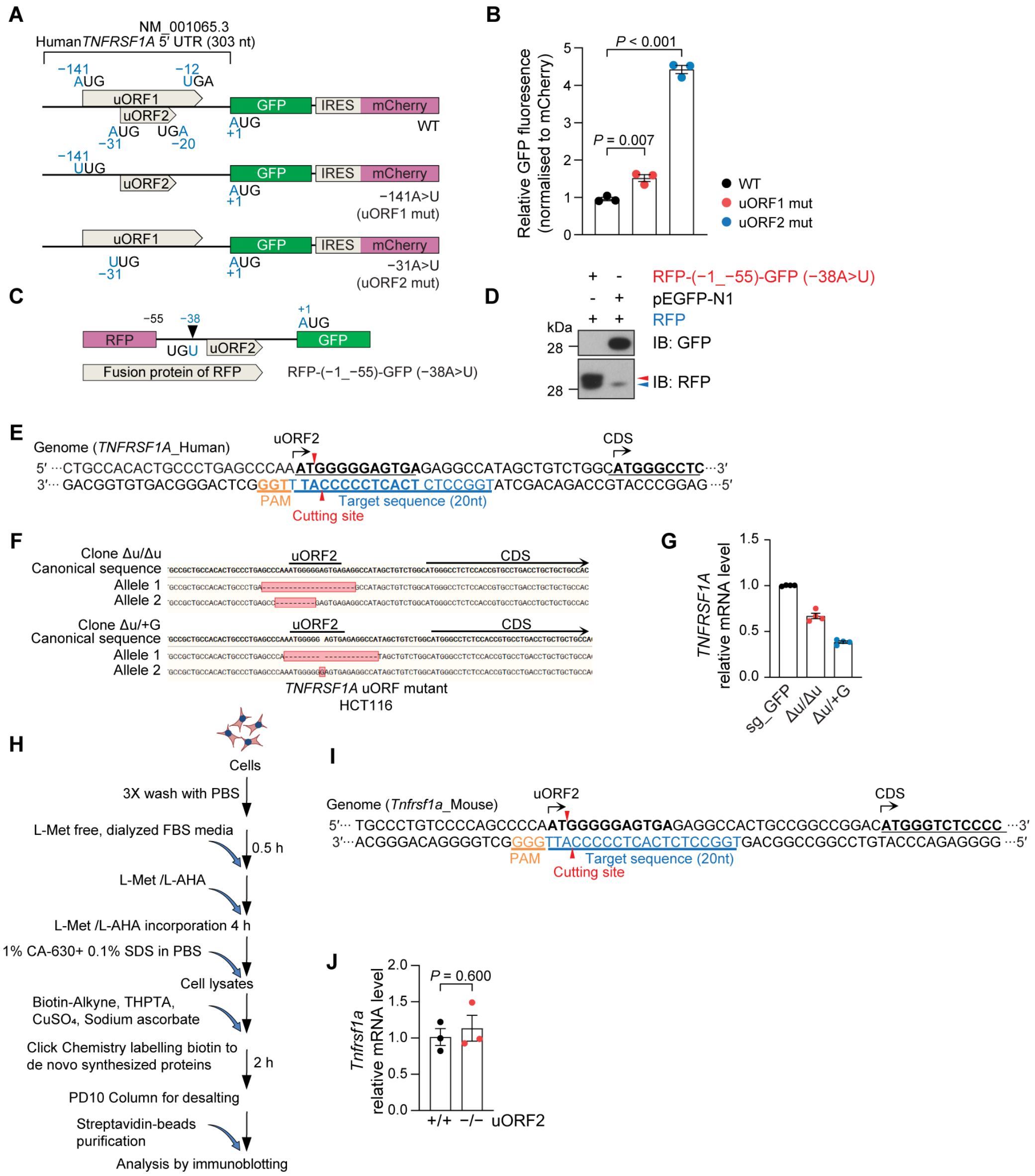

Fig. S1. *TNFRSF1A* uORF2 negatively regulates TNFR1 translation. (**A**) Schematic illustrations of human *TNFRSF1A* 5′ UTR-GFP reporter constructs, including WT and start codon mutants of uORF1 and uORF2. (**B**) GFP fluorescence was measured and normalized to mCherry. HCT116 cells were transfected with the indicated constructs (A) for 24 hours. (**C**) Schematic of the RFP-5′ UTR (human *TNFRSF1A* -1_-55)-GFP fusion reporter construct. (**D**) HCT116 cells were transfected with either the specified GFP reporter construct or the pEGFP-N1 vector for 24 hours. GFP and RFP reporter levels were analyzed by immunoblotting. (**E**) CRISPR-Cas9 target sequences and cutting sites within uORF2 of human *TNFRSF1A*. (**F**) Genomic sequences of alleles in uORF2-mutant HCT116 cells. (**G**) *TNFRSF1A* mRNA levels measured by qRT-PCR, normalized to the housekeeping gene *B2M*. (**H**) Workflow for click-chemistry-based labelling of de novo synthesized proteins. (**I**) CRISPR-Cas9 target sequences and cutting sites within uORF2 of mouse *Tnfrsf1a*. (**J**) *Tnfrsf1a* mRNA levels in MDFs measured by qRT-PCR, normalized to the housekeeping gene *Actb*. Data are presented as the means ± SEM [(B) and (G)] from at least three independent experiments, (D) representative data from three independent experiments with similar results, and (J) one experiment with three biological replicates. Statistical significance was determined by (B) one-way ANOVA with Bonferroni's correction and (J) unpaired two-tailed Student's *t* test.

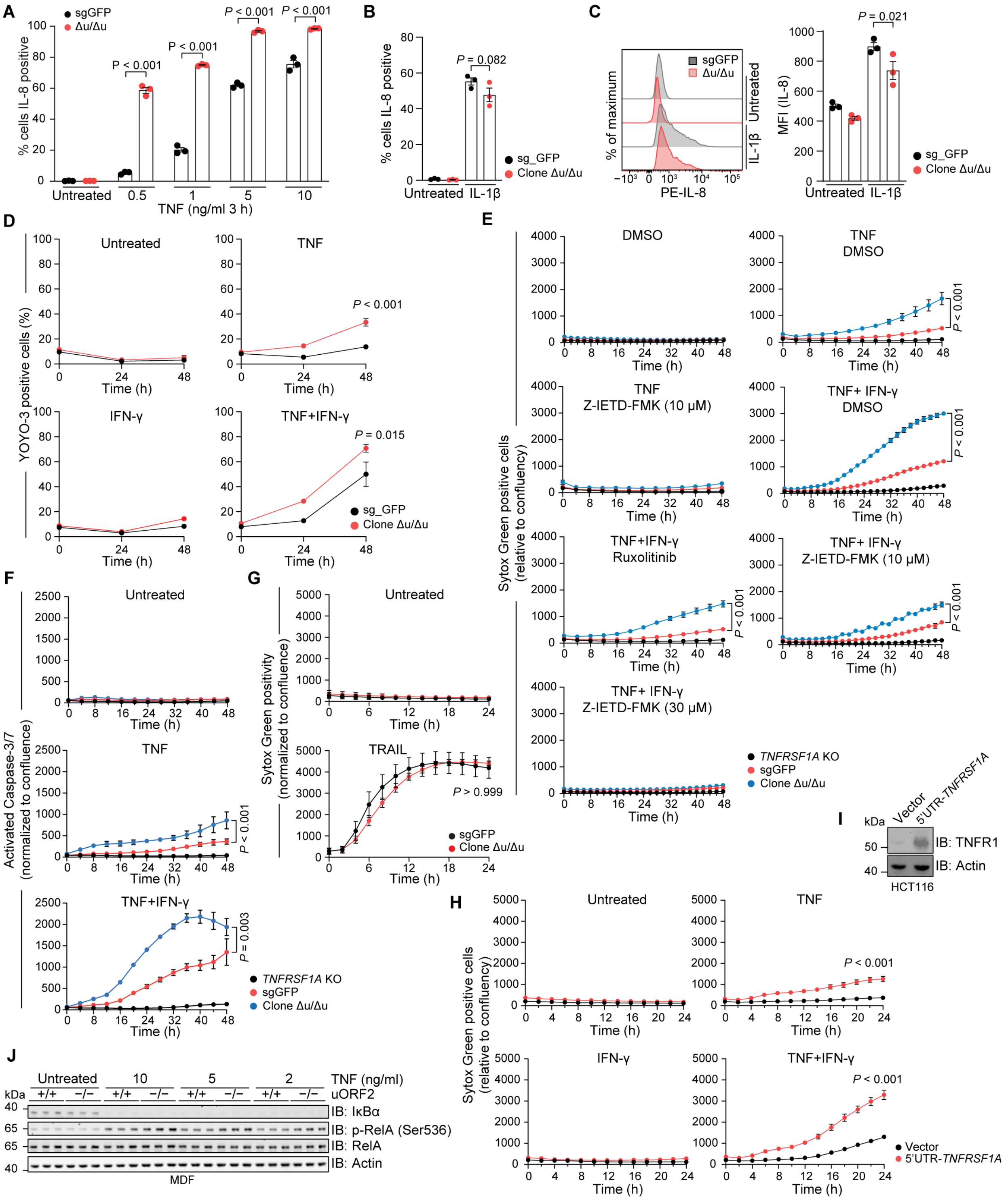

Fig. S2. Disruption of uORF2 enhances TNF-induced cell death. (**A** to **C**) Intracellular IL-8 was analyzed by flow cytometry. Quantification of IL-8+ cells and MFI are shown. HCT116 WT and uORF2-mutant cells were treated with monensin for 1 hour, followed by stimulation with the indicated concentration of TNF (A) or 1 ng/ml of IL-1β (B and C) for 3 hours. (**D**) Cell death was monitored using YOYO-3 at 24 and 48 hours, normalized to Syto21 positivity. HCT116 WT and uORF2-mutant cells were stimulated with 10 ng/ml of TNF, 10 ng/ml of IFN-γ, or both for 48 hours. (**E**) Cell death was monitored in real-time using Sytox Green, normalized to cell confluence. HCT116 WT, uORF2-mutant, and *TNFRSF1A*-knockout cells were pre-treated with DMSO, 5 μM Ruxolitinib, and either 10 μM or 30 μM Z-IETD-FMK for 1 hour, followed by stimulation with 10 ng/mL of TNF, 10 ng/mL of IFN-γ, or both for 48 hours. (**F**) Activated Caspase-3/7 levels were measured by fluorescence and normalized to cell confluence. HCT116 WT, uORF2-mutant, and *TNFRSF1A*-knockout cells were stimulated with 10 ng/mL of TNF or with 10 ng/mL of IFN-γ for 48 hours. (**G**) Cell death was monitored in real-time using Sytox Green, normalized to cell confluence. HCT116 WT and uORF2-mutant cells were treated with 50 ng/mL of TRAIL for 24 hours. (**H** and **I**) (H) Cell death was monitored in real-time using Sytox Green, normalized to cell confluence. (I) TNFR1 overexpression was confirmed by immune blotting. WT control and TNFR1-overexpressing stable HCT116 cells were stimulated with 10 ng/mL of TNF, 10 ng/mL of IFN-γ, or both for 24 hours. (**J**) Primary MDFs from uORF2$^{+/+}$ and uORF2$^{-/-}$ mice were stimulated with the specified TNF concentrations for 15 min. Protein levels were analyzed by immunoblotting with the indicated antibodies. Data are presented as the means ± SEM from [(A) to (H)] at least three independent experiments, (I) representative data from three independent experiments with similar results, and (J) one experiment with three biological replicates. Statistical significance was determined by [(A) to (H)] two-way ANOVA with Bonferroni's correction.

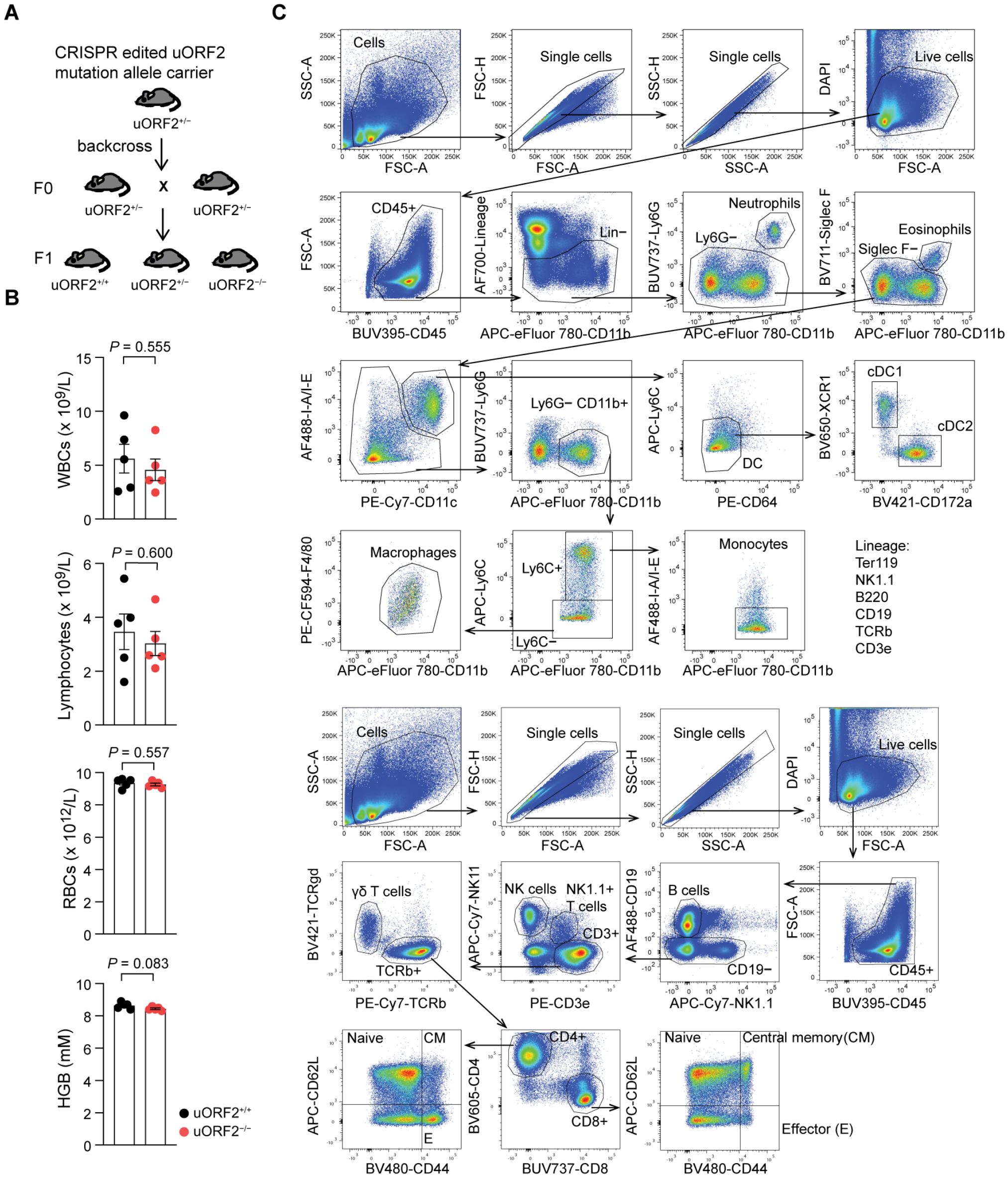

Fig. S3. Characterization of *TNFRSF1A* uORF2-mutant mice. (**A**) Schematic of the breeding strategy used to generate F1 genotypes. (**B**) Blood analysis of white blood cells (WBCs), lymphocytes, red blood cells (RBCs), and hemoglobin (HGB) levels in uORF2$^{+/+}$ and uORF2$^{-/-}$ mice. (**C**) Flow cytometry gating strategy used in immune landscape analysis in the spleen from uORF2$^{+/+}$ and uORF2$^{-/-}$ mice. Data are presented as the means ± SEM from (B) one experiment with five mice per group. Statistical significance was determined by (B) unpaired two-tailed Student's *t* test.

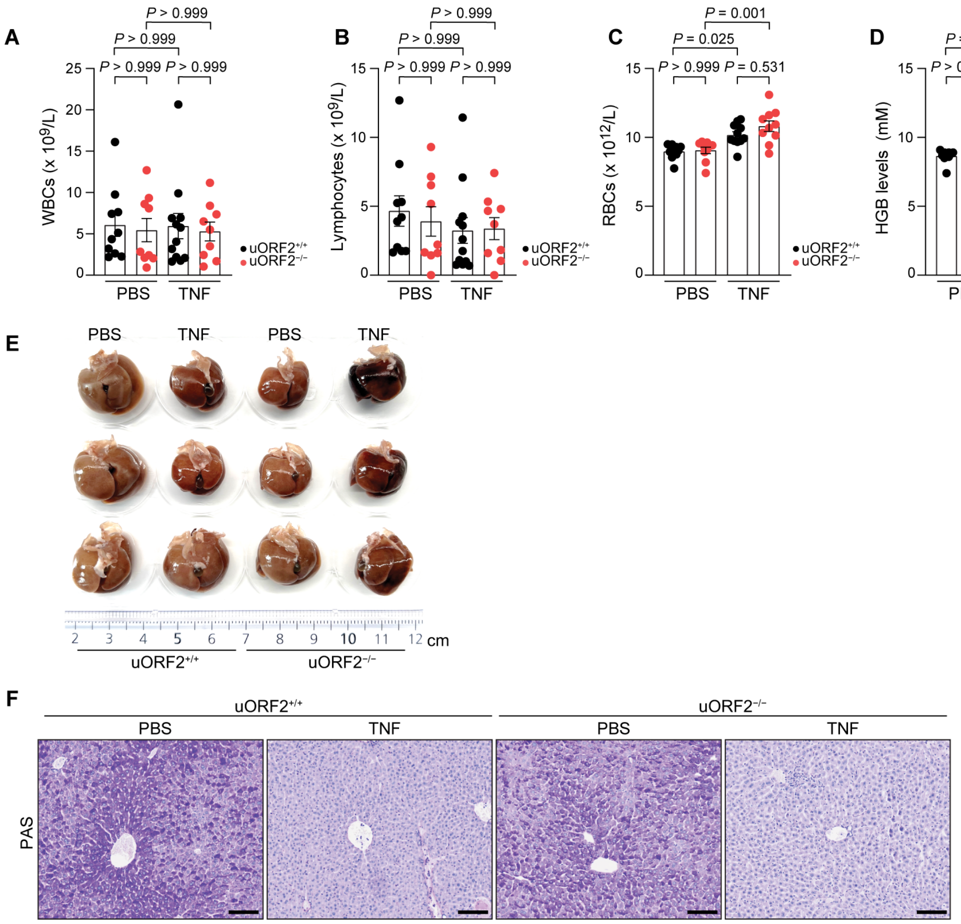

Fig. S4. Disruption of uORF2 enhances TNF signaling in vivo. (**A** to **D**) Blood analysis of uORF2$^{+/+}$ and uORF2$^{-/-}$ mice received 250 µg per kilogram of body weight of recombinant mouse TNF for 2 hours, showing levels of (A) white blood cells (WBCs), (B) lymphocytes, (C) red blood cells (RBCs), and (D) hemoglobins (HGB). (**E**) Liver from the mice from (A to D) were surgically removed, fixed, and photographed. (**F**) Liver sections from panel (E) stained using Periodic Acid–Schiff (PAS) staining. Scale bar: 100 µm. Data are presented as the means ± SEM from [(A) to (D)] combined results of at least two independent experiments with a total of at least eight mice per group, (E) one representative experiment with three mice per group, and (F) representative data from four mice with similar results. Statistical significance was determined by [(A) to (D)] two-way ANOVA with Bonferroni's correction.

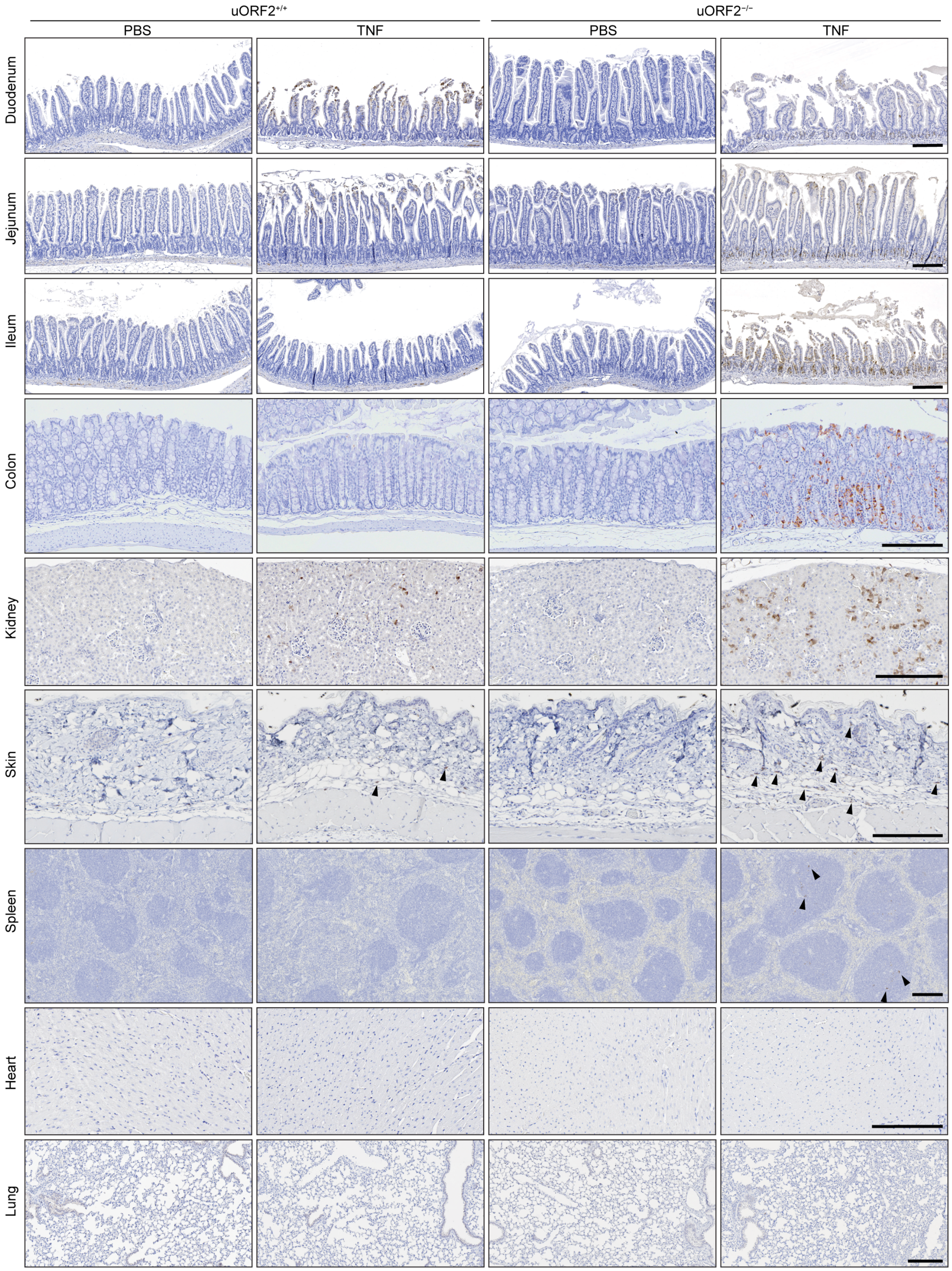

Fig. S5. TNF causes multiple organ damage in *TNFRSF1A* uORF2-mutant mice. uORF2$^{+/+}$ and uORF2$^{-/-}$ mice received 250 µg per kilogram of body weight of recombinant mouse TNF or PBS for 2 hours. Tissue sections were stained for cleaved caspase-3. Arrowheads: cleaved caspase-3 positive cells in the skin and spleen. Scale bar: 200 µm.

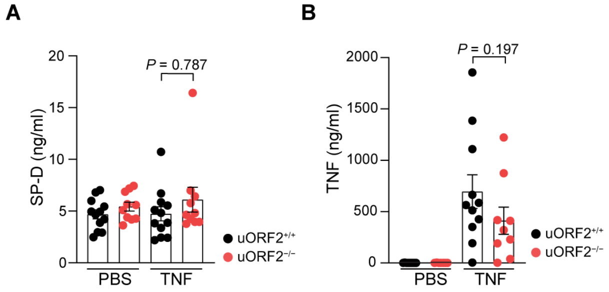

Fig. S6. Surfactant protein D (SP-D) and TNF levels in *TNFRSF1A* uORF2-mutant mice. (**A** and **B**) Plasma protein levels of (A) SP-D and (B) TNF were analyzed by ELISA. Data are presented as the means ± SEM from [(A) and (B)] combined results of at least two independent experiments with a total of at least eight mice per group. Statistical significance was determined by [(A) and (B)] two-way ANOVA with Bonferroni's correction.

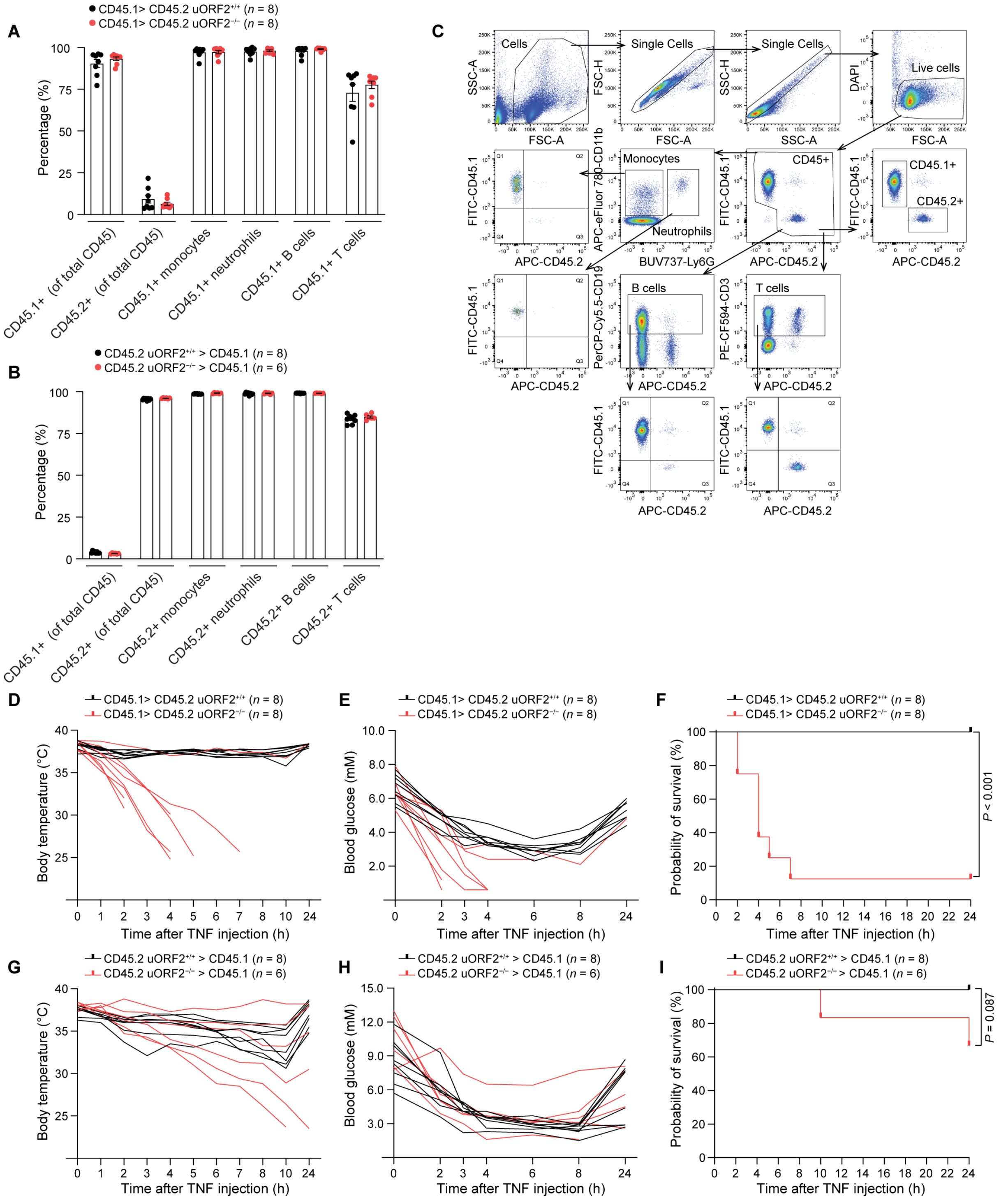

Fig. S7. uORF2-mediated regulation of TNFR1 in non-hematopoietic cells is critical for tissue tolerance to TNF. (**A** and **B**) Reconstitution efficiencies of CD45.1+ (A) and CD45.2+ (B) hematopoietic cells in the indicated host mice were analyzed by flow cytometry. (**C**) Flow cytometry gating strategy used in (A and B). (**D** to **F**) uORF2$^{+/+}$ and uORF2$^{-/-}$ recipient mice reconstituted with WT CD45.1 hematopoietic cells received 250 μg per kilogram of body weight of recombinant mouse TNF. (D) Body temperature, (E) blood glucose levels and (F) survival rate were monitored. 'n' indicates the number of mice per group. **(G** to **I)** WT CD45.1 recipient mice reconstituted with uORF2$^{+/+}$ or uORF2$^{-/-}$ CD45.2 hematopoietic cells received 250 µg per kilogram of body weight of recombinant mouse TNF. (G) Body temperature, (H) blood glucose levels and (I) survival rate were monitored. 'n' indicates the number of mice per group. Data are presented as the means ± SEM from [(A) and (B)] combined results of two independent experiments. Statistical significance was determined by [(F) and (I)] Log-rank (Mantel-Cox) test.

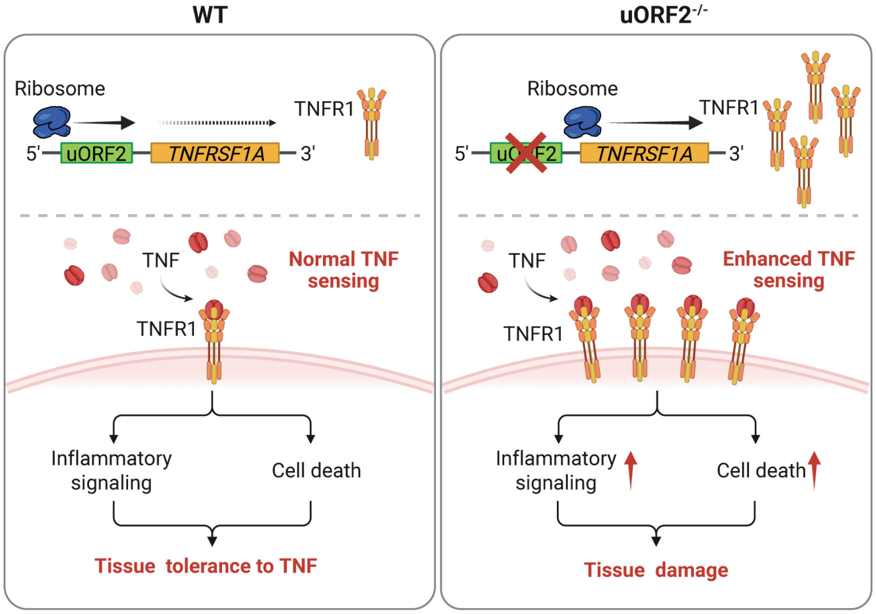

Fig. S8. Schematic model of translational regulation of TNFR1 abundance via uORF2. uORF2 restricts TNFR1 abundance through translational control, thereby limiting TNF-induced proinflammatory signaling and cell death. Disruption of uORF2 increases TNFR1 translation and consequently enhances cellular TNF sensing, which amplifies pro-inflammatory signaling and cell death, ultimately leading to tissue damage. Thus, TNFR1 abundance is rate-limiting for TNF signaling and cell death.

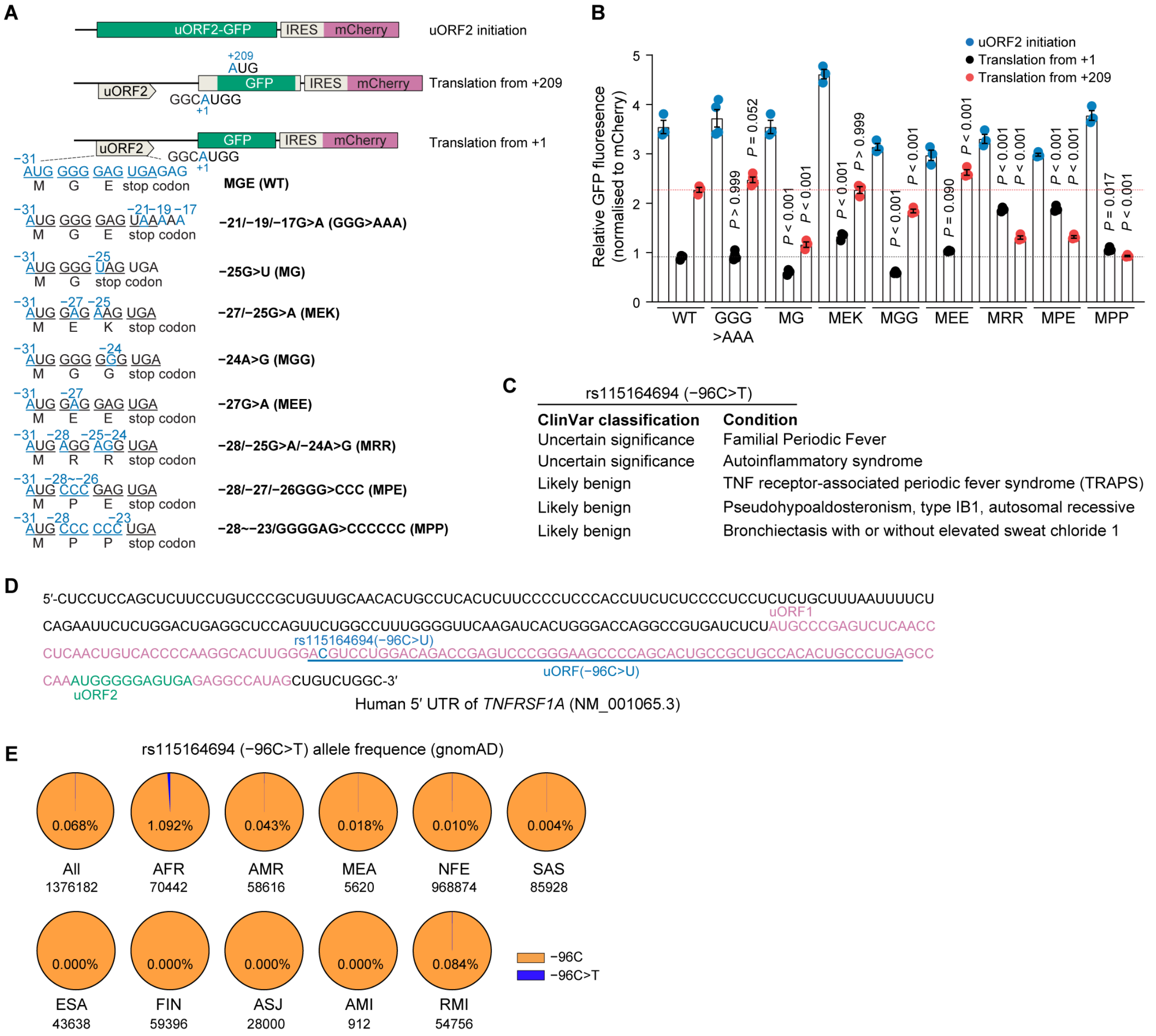

rs115164694 (−96C>T)

ClinVar classification	Condition
Uncertain significance	Familial Periodic Fever
Uncertain significance	Autoinflammatory syndrome
Likely benign	TNF receptor-associated periodic fever syndrome (TRAPS)
Likely benign	Pseudohypoaldosteronism, type IB1, autosomal recessive
Likely benign	Bronchiectasis with or without elevated sweat chloride 1

Fig. S9. uORF2 peptide features influence downstream reinitiation efficiency. (**A**) Schematic overview of human *TNFRSF1A* 5′ UTR-GFP reporter constructs representing translation from uORF2, the main start codon at +1, and the downstream ORF at +209 in WT and mutant constructs. (**B**) HCT116 cells were transfected with the indicated constructs for 24 hours, and GFP fluorescence was measured and normalized to mCherry. (**C**) Summary of SNP rs115164694 (−96C>T) from the ClinVar database. (**D**) Schematic of the human *TNFRSF1A* 5′ UTR (NM_001065.3), showing uORF1 (violet), uORF2 (green), and the neo-uORF introduced by SNP rs115164694 (underlined in blue). (**E**) Allele frequencies of SNP rs115164694 (−96C>T) in different populations based on the gnomAD database: AFR (African/African American), AMR (Admixed American), MID (Middle Eastern), NFE (Non-Finnish European), SAS (South Asian), EAS (East Asian), FIN (Finnish), ASJ (Ashkenazi Jewish), AMI (Amish), and RMI (Remaining Individuals). Data are presented as the means ± SEM from (B) at least three independent experiments. Statistical significance was determined by (B) one-way ANOVA with Bonferroni's correction.

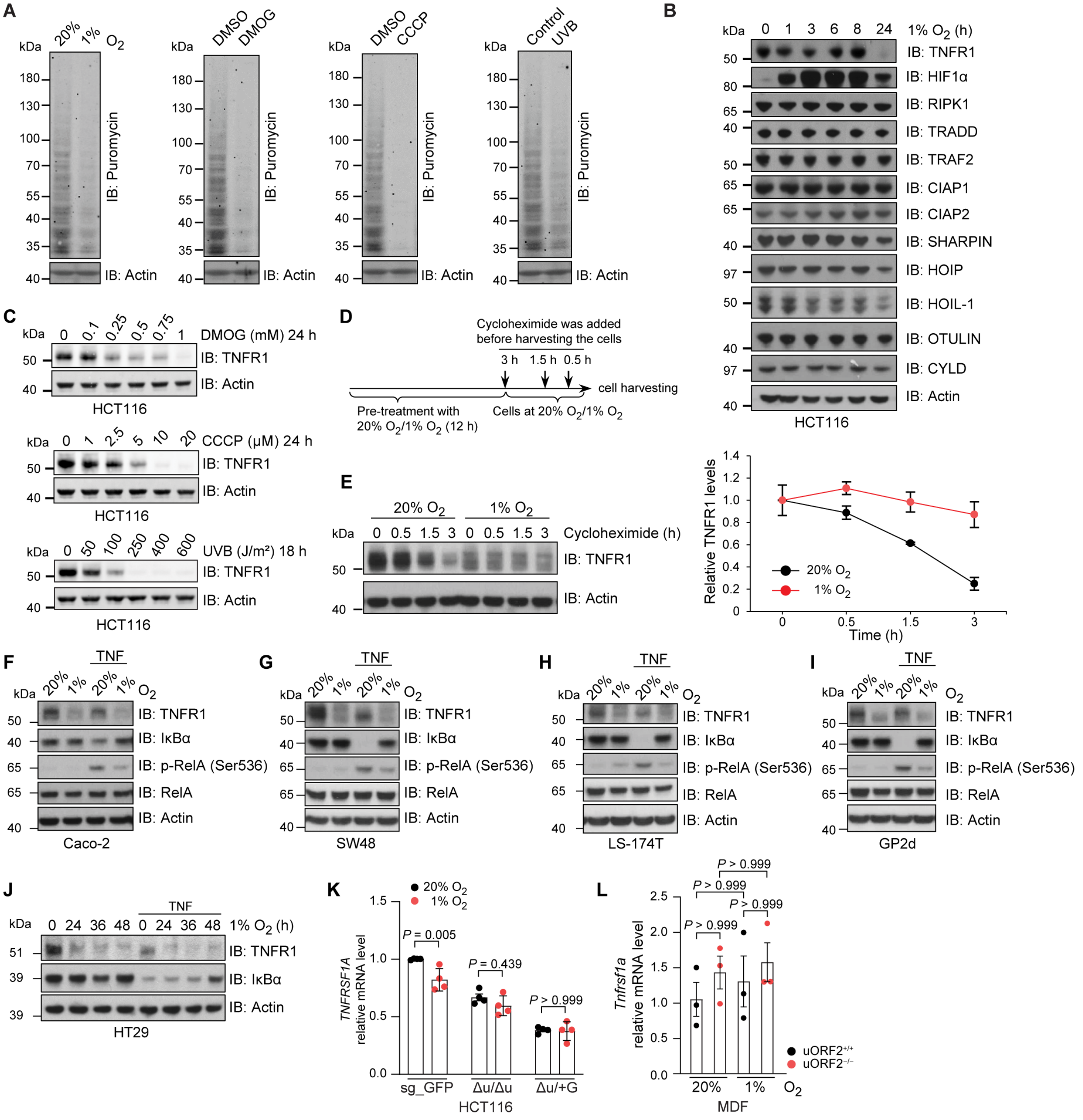

Fig. S10. Cellular stresses downregulate TNFR1 abundance. (**A**) Protein levels were analyzed by immunoblotting. HCT116 cells were treated with 1% oxygen, 0.75 mM DMOG, 10 µM CCCP for 24 hours, or 100 J/m² UVB for 18 hours prior to incubation with 1 µg/ml of puromycin for 30 min. (**B**) Protein levels in HCT116 cells cultured under 1% oxygen were analyzed by immunoblotting at the indicated time points using the specified antibodies. (**C**) TNFR1 protein levels were assessed by immunoblotting. HCT116 cells were treated with DMOG, CCCP, or UVB at the indicated doses and time points. (**D**) Schematic overview of the experimental strategy. (**E**) TNFR1 protein levels were assessed by immunoblotting. HCT116 cells were treated with 100 µg/ml of cycloheximide (CHX) for the indicated times under 20% or 1% oxygen. (**F** to **I**) Protein levels were assessed by immunoblotting. (F) Caco-2, (G) SW48, (H) LS-174T, and (I) GP2d cells were cultured under 1% oxygen for 24 hours, followed by stimulation with 10 ng/ml of TNF for 15 min. (**J**) Protein levels were assessed by immunoblotting. HT29 cells were cultured under 1% oxygen for the indicated times, then stimulated with 10 ng/ml TNF for 15 min. (**K**) *TNFRSF1A* mRNA levels were measured by qRT-PCR and normalized to the housekeeping gene *B2M*. HCT116 WT and uORF2-mutant clones were cultured under 20% or 1% oxygen for 24 h. (**L**) *Tnfrsf1a* mRNA levels were measured by qRT-PCR and normalized to the housekeeping gene *Actb*. uORF2$^{+/+}$ and uORF2$^{-/-}$ MDFs were cultured under 20% or 1% oxygen for 24 hours. Data are presented as the means ± SEM from [(E) and (K)] at least three independent experiments, [(A) to (C), (E) to (J)] representative data from three independent experiments with similar results, and (L) one experiment with three biological replicates. Statistical significance was determined by [(K) and (L)] two-way ANOVA with Bonferroni's correction.

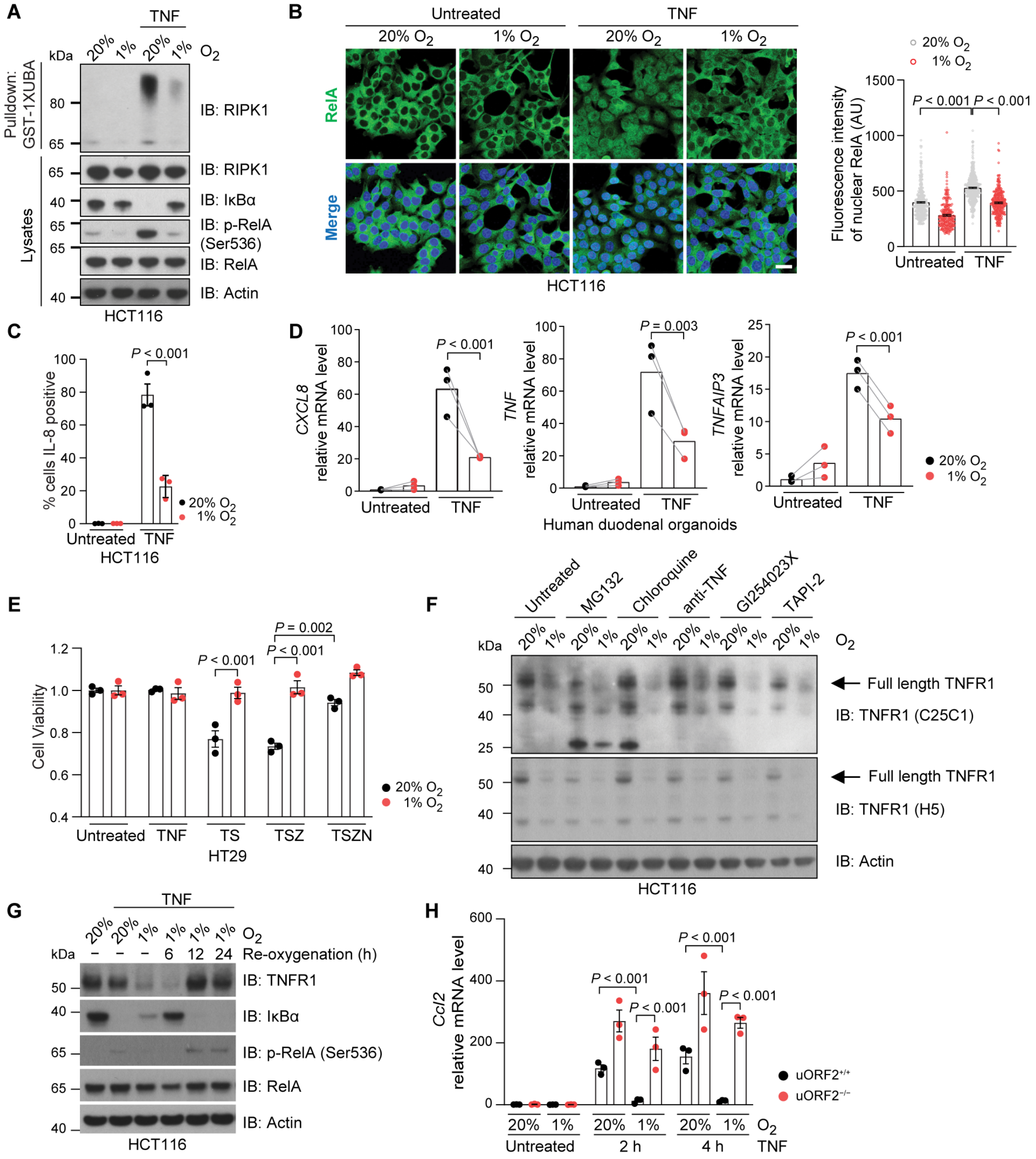

Fig. S11. Hypoxia downregulates TNFR1 and TNF signaling. (**A**) Protein levels were assessed by immunoblotting. Endogenous ubiquitin conjugates were purified from HCT116 cells cultured under 20% or 1% oxygen for 24 hours, then stimulated with 10 ng/ml of TNF for 15 min. (**B**) Cells were stained with anti-RelA antibody (green) and DAPI (blue). Quantification of nuclear RelA fluorescence intensity from individual cells is shown on the right. AU, arbitrary units. HCT116 cells were cultured under 20% or 1% oxygen for 24 hours, then treated with 10 ng/ml of TNF for 30 min. Scale bar: 20 µm. (**C**) Intracellular IL-8 was analyzed by flow cytometry. HCT116 cells were cultured under 20% or 1% oxygen for 20 hours, treated with monensin for 1 hour, followed by 10 ng/ml of TNF for 3 hours. (**D**) *CXCL8*, *TNF*, and *TNFAIP3* mRNA levels were determined by qRT-PCR and normalized to the housekeeping gene *B2M*. Human duodenal organoids derived from three donors were cultured under 20% or 1% oxygen for 48 hours, followed by stimulation with 10 ng/ml of TNF for 3 hours. (**E**) Cell viability was measured using CellTiter-Glo and normalized to untreated controls. HT29 cells were cultured under 20% or 1% oxygen for 48 hours, followed by the indicated treatments for an additional 4 hours. TNF (5 ng/ml), Compound A (CpA, 100 nM), Z-VAD-FMK (20 μM), and Nec1s (10 μM) were used. Treatment groups: TS (TNF + CpA), TSZ (TNF + CpA + Z-VAD-FMK), TSZN (TNF + CpA + Z-VAD-FMK + Nec1s). (**F**) TNFR1 protein levels were determined by immunoblotting using two monoclonal antibodies. HCT116 cells were cultured under 20% or 1% oxygen for 18 hours, followed by treatment with MG132 (20 μM) or chloroquine (60 μM) for an additional 6 hours before harvesting. Alternatively, HCT116 cells were treated with neutralizing anti-TNF antibody (1 μg/ml, MAB210, R&D Systems, Clone 1825), G1254023X (10 μM), or TAPI2 (100 μM) and cultured under 20% or 1% oxygen for 24 hours. (**G**) Protein levels were assessed by immunoblotting. HCT116 cells were cultured under 20% or 1% oxygen for 24 hours, followed by re-oxygenation for the indicated times, then stimulated with 10 ng/ml of TNF for 15 min. (**H**) *Ccl2* mRNA levels were quantified by qRT-PCR, normalized to the housekeeping gene *Actb*. uORF2$^{+/+}$ and uORF2$^{-/-}$ MDFs were cultured under 20% or 1% oxygen for 20 hours, then stimulated with 10 ng/ml of TNF at the indicated times. Data are presented as the means ± SEM from [(C) and (E)] three independent experiments, [(A), (B), (F), and (G)] representative data from three independent experiments with similar results, (H) one experiment with three biological replicates, and (D) one experiment with three donors. Statistical significance was determined by [(B) to (E), (H)] two-way ANOVA with Bonferroni's correction.

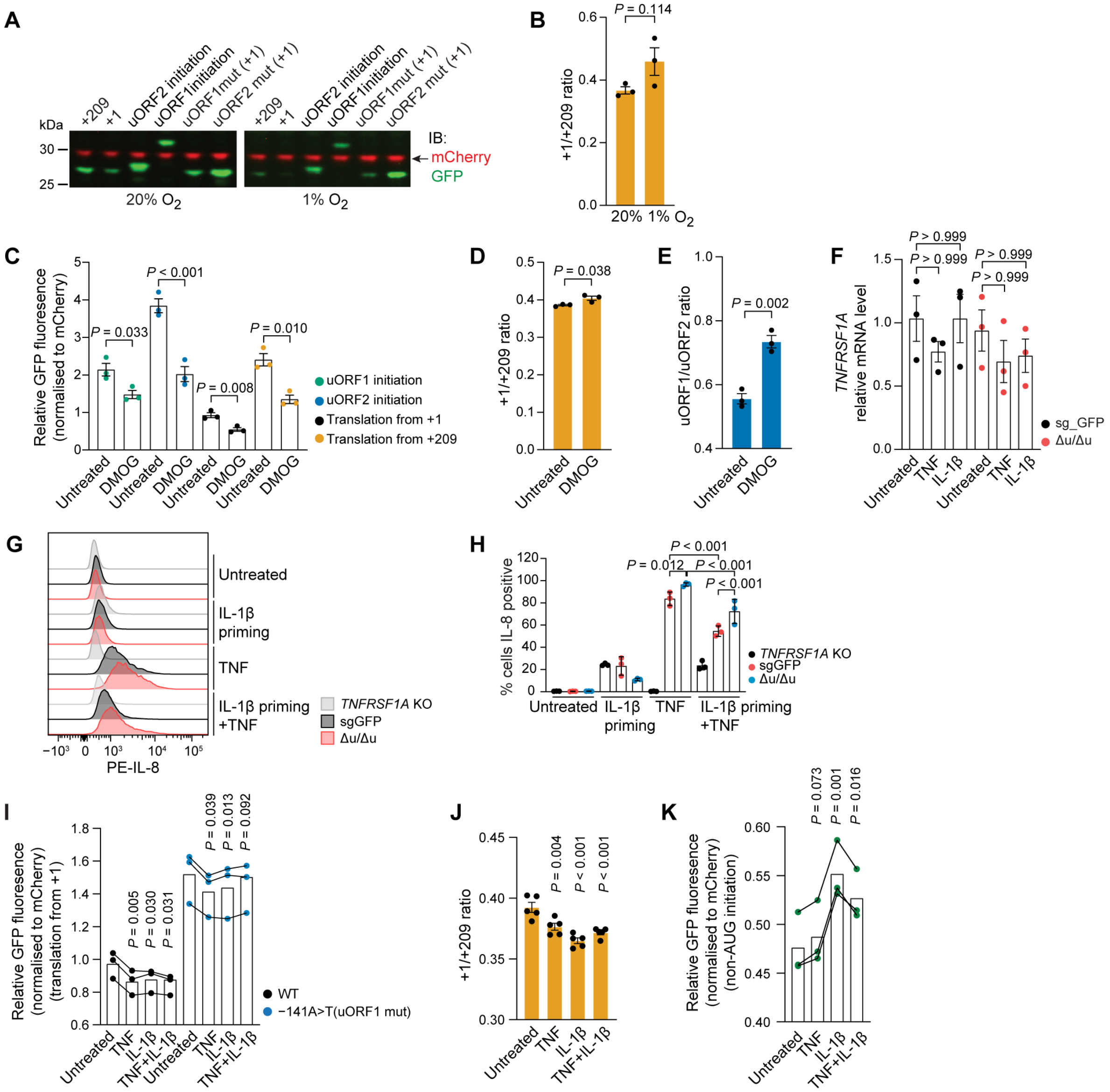

Fig. S12. Stress induces uORF1 translation initiation. (**A** and **B**) HCT116 cells were transfected with the indicated reporter constructs. One hour later, cells were cultured under 20% or 1% oxygen for 24 hours. (A) GFP and mCherry were assessed by fluorescence-based immunoblotting. (B) Ratios of translation at +1 versus +209 are shown. (**C** to **E**) HCT116 cells were transfected with the indicated reporter constructs. One hour later, cells were treated with or without 0.75 mM DMOG for an additional 24 hours. (C) GFP fluorescence was measured and normalized to mCherry. Ratios of translation at (D) +1 versus +209 and (E) initiations of uORF1 versus uORF2 are shown. (**F**) *TNFRSF1A* mRNA levels were measured by qRT-PCR and normalized to the housekeeping gene *ACTB*. HCT116 WT and uORF2-mutant (Δu/Δu) cells were treated with 10 ng/ml of TNF, 10 ng/ml of IL-1β, or a combination of both for 24 hours. (**G** and **H**) (G) Representative of intracellular IL-8 MFI and (H) quantification of IL-8-positive cells are shown. Cells were pretreated with 10 ng/ml of IL-1β for 24 hours, then stimulated with 10 ng/ml of TNF for additional 3 hours. Related to Fig 6L. (**I** to **K**) HCT116 cells were transfected with the indicated reporter constructs. One hour later, cells were treated with 10 ng/ml of TNF, 10 ng/ml of IL-1β, or a combination of both for 24 hours. Translation from the (I) +1 start site, (J) ratios of translation at +1 versus +209, and (K) non-AUG initiation were measured and normalized to mCherry. Data are presented as the means ± SEM from [(B) to (F), and (H) to (K)] at least three independent experiments, and [(A) and (G)] representative data from three independent experiments with similar results. Statistical significance was determined by [(C), (I) to (K)] one-way ANOVA with Bonferroni's correction, [(F) and (H)] two-way ANOVA with Bonferroni's correction, and [(B), (D), and (E)] unpaired two-tailed Student's *t* test.

Table S1. List of flow cytometry antibodies.

Name	Supplier	Cat. no.	Monoclonal number	Dilution	Working concentration
AF700 anti-mouse NK1.1	BD Biosciences	560515.00	PK136	1:100	2 μg/ml
AF700 anti-mouse CD19	BD Biosciences	557958.00	1D3	1:100	2 μg/ml
PerCP-Cy5.5 anti-mouse CD19	BD Biosciences	561113.00	1D3	1:200	1 μg/ml
BV711 anti-mouse Siglec F	BD Biosciences	740764.00	E50-2440	1:200	1 μg/ml
PE-CF594 anti-mouse CD3e	BD Biosciences	562286.00	145-2C11	1:200	1 μg/ml
BV421 anti-mouse CD172a/SIRPa	BD Biosciences	740071.00	P84	1:200	1 μg/ml
PE-CF594 anti-mouse F4/80	BD Biosciences	565613.00	T45-2342	1:200	1 μg/ml
APC anti-mouse Ly6C	BD Biosciences	560595.00	AL-21	1:200	1 μg/ml
BUV395 anti-mouse CD45	BD Biosciences	564279.00	30-F11	1:200	1 μg/ml
AF488 anti-mouse I-A/I-E	BD Biosciences	562352.00	M5/114.15.2	1:400	0.5 μg/ml
BUV737 anti-mouse Ly6G	BD Biosciences	741813.00	1A8	1:400	0.5 μg/ml
BV605 anti-mouse CD4	BD Biosciences	743156.00	GK1.5	1:200	1 μg/ml
BUV737 anti-mouse CD8	BD Biosciences	612759.00	53-6.7	1:200	1 μg/ml
APC-Cy7 anti-mouse NK1.1	BD Biosciences	560618.00	PK136	1:200	1 μg/ml
BV480 anti-mouse CD44	BD Biosciences	566116.00	IM7	1:200	1 μg/ml
BV786 anti-mouse CD69	BD Biosciences	564683.00	H1.2F3	1:200	1 μg/ml
APC anti-mouse CD62L	BD Biosciences	561919.00	MEL-14	1:200	1 μg/ml
BV421 anti-mouse TCRgd	BD Biosciences	562892.00	GL3	1:200	1 μg/ml
FITC anti-mouse CD19	BD Biosciences	557398.00	1D3	1:200	1 μg/ml
PE-Cy7 anti-mouse TCRb	BD Biosciences	560729.00	H57-597	1:400	0.5 μg/ml
PerCP anti-mouse CD19	BD Biosciences	561113.00	1D3	1:100	2 μg/ml
APC anti-human TNFR1	Biolegend	369906.00	W15099A	1:100	1 μg/ml
APC Mouse IgG2a, κ Isotype Ctrl	Biolegend	400222.00	MOPC-173	1:100	1 μg/ml
APC anti-mouse TNFR1	Biolegend	113006.00	55R-286	1:100	2 μg/ml
APC hamster IgG Isotype Ctrl	Biolegend	400912.00	HTK888	1:100	2 μg/ml
AF700 anti-mouse CD3e	Biolegend	100216.00	17A2	1:100	5 μg/ml
BV650 anti-mouse XCR1	Biolegend	148220.00	ZET	1:200	2 μg/ml
FITC anti-mouse CD45.1	Biolegend	110705.00	A20	1:200	2.5 μg/ml
APC anti-mouse CD45.2	Biolegend	109814.00	104.00	1:200	1 μg/ml
PE anti-human IL-8	ThermoFisher Scientific	12-8088-42	8CH	1:100	0.25 μg/ml
AF700 anti-mouse Ter19	ThermoFisher Scientific	56-5921-82	TER-119	1:100	2 μg/ml
AF700 anti-mouse B220	ThermoFisher Scientific	56-0452-82	RA3-6B2	1:100	2 μg/ml
AF700 anti-mouse TCRb	ThermoFisher Scientific	56-5961-82	H57-597	1:100	2 μg/ml
PE anti-mouse CD64	ThermoFisher Scientific	12-0641-82	12-0641-82	1:100	2 μg/ml
APC-eFluor 780 anti-mouse CD11b	ThermoFisher Scientific	47-0112-82	M1/70	1:400	0.5 μg/ml
PE-Cy7 anti-mouse CD11c	ThermoFisher Scientific	25-0114-81	N418	1:600	0.33 μg/ml
PE anti-mouse CD3e	ThermoFisher Scientific	12-0031-81	145-2C11	1:200	1 μg/ml

Table S2. List of immunohistochemistry antibodies.

Name	Supplier	Cat. no.	Monoclonal number	Host	Dilution	Working concentration
anti-CD3	Abcam	ab16669	SP7	rabbit	1:150	0.06 µg/ml
anti-Cl. Caspase-3 (Asp175)	Cell Signaling	9661	Polyclonal	rabbit	1:400	0.13 µg/ml
anti-F4/80	BioLegend	123101	BM8	rat	1:200	2.5 µg/ml
anti-B220	BioLegend	103201	RA3-6B2	rat	1:100	5 µg/ml
anti-Ly6G	BioLegend	127601	127601	rat	1:200	2.5 µg/ml
anti-CD45	ThermoFisher Scientific	14-0451-82	30-F11	rat	1:200	2.5 µg/ml
IHC Detection Reagent (HRP, rabbit)	Cell Signaling	8114	N.A.	goat	ready to use	
IHC Detection Reagent (HRP,rat)	Cell Signaling	72838	N.A.	goat	ready to use	

Table S3. List of immunoblotting antibodies.

Name	Supplier	Cat. no.	Monoclonal number	Host	Dilution	Working concentration
anti-HOIP	Aviva Systems Biology	ARP43241_P050	N.A.	rabbit	1:1000	0.7 µg/ml
anti-HIF1α	BD Biosciences	610958	54	mouse	1:2000	0.125 µg/ml
anti-Caspase 8	Cell Signaling	4790	D35G2	rabbit	1:1000	0.159 µg/ml
anti-Cleaved Caspase-8 (Asp374)	Cell Signaling	9496	18C8	rabbit	1:1000	0.133 µg/ml
anti-CYLD	Cell Signaling	8462	D1A10	rabbit	1:1000	0.044 µg/ml
anti-IkB-alpha	Cell Signaling	9242	N.A.	rabbit	1:1000	N.A.
anti-MLKL (mouse specific)	Cell Signaling	37705	D6W1K	rabbit	1:1000	0.209 µg/ml
anti-OTULIN	Cell Signaling	14127	N.A.	rabbit	1:1000	N.A.
anti-phospho-MLKL (S345) (mouse specific)	Cell Signaling	37333	D6E3G	rabbit	1:1000	0.056 µg/ml
anti-phospho-RelA (S536)	Cell Signaling	3033	93H1	rabbit	1:1000	0.057 µg/ml
anti-phospho-RIPK1 (S166) (human specific)	Cell Signaling	65746	D1L3S	rabbit	1:1000	0.181 µg/ml
anti-phospho-RIPK1 (S166) (mouse specific)	Cell Signaling	53286	E7G6O	rabbit	1:1000	0.225 µg/ml
anti-phospho-RIPK3 (T231/S232)	Cell Signaling	91702	E7S1R	rabbit	1:1000	0.140 µg/ml
anti-RelA	Cell Signaling	8242	D14E12	rabbit	1:1000	0.208 µg/ml
anti-RIPK1	Cell Signaling	3493S	D94C12	rabbit	1:1000	0.004 µg/ml
anti-S6	Cell Signaling	2217	5G10	rabbit	1:1000	N.A.
anti-TNFR1	Cell Signaling	3736	C25C1	rabbit	1:1000	0.029 µg/ml
anti-TNFR1 (rodent specific)	Cell Signaling	13377	D3I7K	rabbit	1:1000	0.29 µg/ml
anti-c-IAP1	ENZO	ALX-803-335	1E1-1-10	rat	1:4000	1 µg/ml
anti-c-IAP2	ENZO	ALX-803-341	16E-6-3	rat	1:2000	1 µg/ml
anti-linear ubiquitin (Met1)	Merck	ZRB2114	1E3	rabbit	1:20000	N.A.
anti-Puromycin	Merck	MABE342	4G11	mouse	1:12500	N.A.
anti-Actin	Merck	MAB1501	C4	mouse	1:20000	N.A.
anti-RIPK3	Novus biologicals	NBP1-77299	N.A.	rabbit	1:2000	0.5 µg/ml
anti-SHARPIN	Proteintech	14626-1-AP	N.A.	rabbit	1:2000	0.325 µg/ml
anti-GFP	ProteinTech	66002-1-Ig	1E10H7	mouse	1:100000	0.02 µg/ml
anti-RFP	Proteintech	26765-1-AP	N.A.	rabbit	1:3000	0.233 µg/ml
anti-HOIL-1	Santa Cruz	sc-365523	E-2	mouse	1:1000	0.2 µg/ml
anti-TNFR1	Santa Cruz	sc-7883	H-5	mouse	1:1000	0.2 µg/ml
anti-TRADD	Santa Cruz	sc-7868	N.A.	rabbit	1:1000	0.2 µg/ml
anti-TRAF2	Santa Cruz	sc-876	N.A.	rabbit	1:1000	0.2 µg/ml
Streptavidin-HRP	Abcam	ab7403	N.A.	N/A	1:10000	0.1 µg/ml
anti-mouse-HRP	Cell Signaling	7076	N.A.	horse	1:3000	N.A.
anti-rabbit-HRP	Cell Signaling	7074	N.A.	goat	1:3000	N.A.
anti-mouse-IRDye® 800CW	LI-COR	926-32210	N.A.	goat	1:20000	0.05 µg/ml
anti-rabbit-IRDye® 800CW	LI-COR	926-32211	N.A.	goat	1:20000	0.05 µg/ml
anti-mouse-IRDye® 680RD	LI-COR	926-68070	N.A.	goat	1:20000	0.05 µg/ml
anti-rat-HRP	ThermoFisher Scientific	31470	N.A.	goat	1:10000	0.08 µg/ml

Table S4. List of qRT-PCR primers.

Name	**Sequence**
human *CXCL8* Forward	TCTGGCAACCCTAGTCTGCT
human *CXCL8* Reverse	AAACCAAGGCACAGTGGAAC
human *TNF* Forward	TGCTGCAGGACTTGAGAAGA
human *TNF* Reverse	GAGGAAGGCCTAAGGTCCAC
human *TNFAIP3* Forward	ATGCACCGATACACACTGGA
human *TNFAIP3* Reverse	GGATGATCTCCCGAAACTGA
human *TNFRSF1A* Forward	TCACCGCTTCAGAAAACCACC
human *TNFRSF1A* Reverse	GGTCCACTGTGCAAGAAGAGA
human *B2M* Forward	GAGGCTATCCAGCGTACTCCA
human *B2M* Reverse	CGGCAGGCATACTCATCTTTT
human *ACTB* Forward	TCACCCACATGTGCCCATCTACGA
human *ACTB* Reverse	CAGCGGAACCGCTCATTGCCAATG
mouse *Tnfrsf1a* Forward	GGGCACCTTTACGGCTTCC
mouse *Tnfrsf1a* Reverse	TCTCCTTACAGGGGATTGTCAC
mouse *Tnf* Forward	CATCTTCTCAAAATTCGAGTGACAA
mouse *Tnf* Reverse	TGGGAGTAGACAAGGTACAACCC
mouse *Il1b* Forward	TGTAATGAAAGACGGCACACC
mouse *Il1b* Reverse	TCTTCTTTGGGTATTGCTTGG
mouse Cxcl1 Forward	CTGGGATTCACCTCAAGAACATC
mouse *Cxcl1* Reverse	CAG GGT CAA GGC AAG CCT C
mouse *Ccl2* Forward	TTAAAAACCTGGATCGGAACCAA
mouse *Ccl2* Reverse	GCATTAGCTTCAGATTTACGGGT
mouse *Nfkbia* Forward	TGAAGGACGAGGAGTACGAGC
mouse *Nfkbia* Reverse	TTCGTGGATGATTGCCAAGTG
mouse *Tnfaip3* Forward	GAACAGCGATCAGGCCAGG
mouse *Tnfaip3* Reverse	GGACAGTTGGGTGTCTCACATT
mouse *Actb* Forward	GGCTGTATTCCCCTCCATCG
mouse *Actb* Reverse	CCAGTTGGTAACAATGCCATGT

Data file S1. (.xlsx)
List of putative off-target sites in uORF2-mutant mice validated as negative via genomic sequencing.

Data file S2. (.xlsx)
List of uORF features in canonical immune receptor genes.

Data file S3. (.pdf)
Uncropped immunoblots.

Data file S4. (.xlsx)
Source data file.